Harvey, E., Kirk, V., Osinga, H. M., Sneyd, J., & Wechselberger, M. (2010). Understanding anomalous delays in a model of intracellular calcium dynamics.

Understanding anomalous delays in a model of intracellular calcium dynamics*

Emily Harvey† Vivien Kirk†
Hinke M. Osinga§ James Sneyd† Martin Wechselberger¶

July 31, 2010

Abstract

In many cell types, oscillations in the concentration of free intracellular calcium ions are used to control a variety of cellular functions. It has been suggested [16] that the mechanisms underlying the generation and control of such oscillations can be determined by means of a simple experiment, whereby a single exogenous pulse of inositol trisphosphate (IP_3) is applied to the cell. However, more detailed mathematical investigations [6] have shown that this is not necessarily always true, and that the experimental data are more difficult to interpret than first thought. Here, we use geometric singular perturbation techniques to study the dynamics of Class I, Class II and Hybrid models of calcium oscillations. In particular, we show how recently developed canard theory for singularly perturbed systems systems with three or more slow variables [19] applies to these calcium models and how the presence of a curve of folded singularities and corresponding canards can result in anomalous delays in the response of these models to a pulse of IP_3.

Oscillations in the concentration of cytoplasmic free calcium are a signalling mechanism in practically every cell type, and control a wide variety of cellular functions, from secretion and movement to cell differentiation and gene expression [2]. It is thus important to understand the mechanisms underlying the generation and control of such oscillations. Previous work has shown that calcium oscillations often arise as the result of one of two principal mechanisms, so-called Class I and Class II mechanisms. It has been claimed [16]

---

*This work was supported by the Marsden Fund, NZ

†Department of Mathematics,University of Auckland, Private Bag 92019, Auckland, NZ

§Department of Engineering Mathematics, University of Bristol, Bristol BS8 1TR, UK

¶School of Mathematics and Statistics, University of Sydney, NSW, Australia (corresponding author)

that a simple experiment (a single exogenous pulse of inositol trisphosphate, or IP$_3$) is able to distinguish between whether or not calcium oscillations in a cell are a result principally of a Class I or a Class II mechanism. However, more detailed mathematical studies of these models [6] have shown that the situation is more complex than appeared at first, and there are situations in which a Class I model can look remarkably like a Class II model, making interpretation of the experimental data ambiguous and difficult. Here we perform a detailed mathematical study of Class I and Class II models, investigate how they respond to a pulse of IP$_3$, and provide a detailed explanation of why Class I and Class II models cannot necessarily be easily distinguished by the IP$_3$ pulse experiment. It turns out that this is related to the phenomenon of canards in systems with three slow variables, the theory of which has been developed recently [19].

1 Introduction

Calcium is one of the main secondary signalling messengers in living cells [2]. Changes in calcium concentration usually take the form of oscillations, in which the free cytoplasmic calcium concentration alternately rises and falls, the signal being encoded in the frequency of the oscillation.

There is general agreement over the first steps of the process that results in calcium oscillations [11]: binding of an agonist to a cell-surface receptor initiates a series of reactions that ends in the formation of the intracellular second messenger, inositol (1,4,5)-trisphosphate (IP$_3$), which opens IP$_3$ receptors (which are also calcium channels) on the membrane of the endoplasmic reticulum (ER), leading to the release of calcium from that internal store. Oscillations in the cytoplasmic calcium concentration occur as calcium is alternatively released from, and pumped into, the ER.

The exact mechanisms that cause such cyclical release and reuptake remain controversial. There are two principal hypotheses: *Class I models* claim that the oscillations occur as a result of calcium feedback on the IP$_3$ receptor (IPR) [16]. Since calcium can activate the IPR quickly, release of calcium from the ER is a positive feedback process. However, on a slower time scale, calcium also inactivates the IPR, thus, giving slower negative feedback. It is well known from many models [11] that fast positive feedback followed by slower negative feedback can generate oscillations. However, the biochemistry of calcium oscillations is far more complex than merely feedback on the IPR. Indeed, calcium itself affects the rates of production and degradation of IP_3, leading again to positive and negative feedback on the release of calcium. This second feedback loop is incorporated in *Class II models* and is the principal mechanism underlying oscillations in some cell types [16].

However in real cells, both Class I and Class II mechanisms will usually occur, in which case one has to use a *Hybrid model* that includes both mechanisms. One of the important current questions in the study of calcium dynamics is whether, in each cell type, both mechanisms are equally important, or whether one mechanism, Class I or Class II, dominates and hence drives the oscillations.

One possible way to distinguish between Class I and Class II mechanisms was introduced in [16]. There it was shown that, in a variety of Class I models, an exogenous pulse of IP_3 causes a temporary increase in oscillation frequency, while in Class II models, an identical pulse of IP_3 causes a phase lag, with the next peak occurring after a delay. These types of response are illustrated in Fig. 1(a) and (c), respectively, with time series of the concentrations of calcium and IP_3 generated from the Atri model (1).

The model predictions were tested in two cell types, namely, in mouse pancreatic acinar cells and mouse airway smooth muscle cells [16]. The authors concluded that calcium oscillations generated by cholecystokinin in pancreatic acinar cells are the result of a Class II mechanism, while calcium oscillations generated by methacholine in mouse airwave smooth muscle are the result of a Class I mechanism.

Unfortunately, the story is not as simple as presented in [16]. As reported in [6], under certain conditions a Class I model can respond to an IP_3 pulse by exhibiting a small number of faster oscillations, followed by a long delay, before recovering to the initial oscillatory pattern. This is a highly non-intuitive result: in Class I models the oscillation frequency is an increasing function of the IP_3 concentration (assuming that transients have died away), and thus a temporary increase in the IP_3 concentration might be expected to lead to a temporary increase in oscillation frequency, not to a long delay. Although this is usually what happens, sometimes the pulse in IP_3 causes the response described above, i.e., a small number of faster oscillations, followed by a long delay before oscillations appear again. A specific example of such a response can be seen in Fig. 1(b). We term this response an *anomalous delay.* The occurrence of anomalous delays under certain circumstances creates problems for the interpretation of the experimental results. If a Class I model can sometimes respond like a Class II model, then how can the two model types be distinguished using pulses of IP_3?

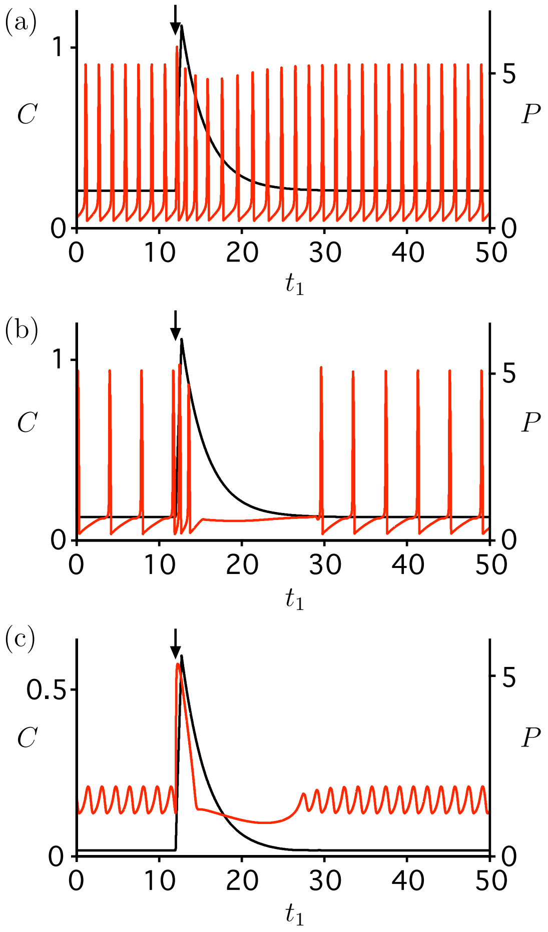

Figure 1: Responses of the Atri model (1) with $\epsilon = 0.01$ to IP$_3$ pulses. The IP$_3$ pulse is applied at the time indicated by the arrow, with the explicit form of the pulse given by (2), assuming that any transients have died out before the time trace is started. Each panel shows the time series of the concentrations C of calcium (red curve) and P of IP$_3$ (black curve). (a) Class I: $\alpha = 0$, $\hat{\tau} = 0.48$ ($\tau = 2\,s$) for $\hat{\nu} = 0.40$ ($\nu = 0.96$) and other parameter values as in Table 1. (b) Class I: as in panel (a) except with $\hat{\nu} = 0.233$ ($\nu = 0.56$). (c) Class II: $\alpha = 1$, $\hat{\tau} = 0$ ($\tau = 0$) for $\hat{\nu} = 0.417$ ($\nu = 1.00$).

1.1 Multiple time scales in a representative model

A first step towards a better understanding of the model dynamics is presented in our recent work [9]. Based on geometric singular perturbation theory (GSPT) [4, 8, 10, 17, 18], we showed in that paper that the intrinsic dynamics of a model of intracellular calcium dynamics is mainly controlled by distinct time scales describing the (slow or fast) evolution of the model variables relative to each other. This inherent multiple time-scale structure provides us with a simple necessary condition for Class I and Class II dynamics by calculating a dimensionless quantity $\epsilon \ll 1$ representing the ratio of the different time scales involved.

This is most easily illustrated using a representative model, the Atri model [1, 6], which we will use as an example throughout this paper, and which has the following dimensionless form [9]:

$$\left\{\begin{array}{rclcl}\epsilon\,\dfrac{dC}{dt_1} & = & \bar{J}_{\text{release}} - \bar{J}_{\text{serca}} + \epsilon\,(\bar{J}_{\text{in}} - \bar{J}_{\text{pm}}) & = & f(C, C_t, r, P, \epsilon),\\ \dfrac{dC_t}{dt_1} & = & \bar{J}_{\text{in}} - \bar{J}_{\text{pm}} & = & g_1(C),\\ \dfrac{dr}{dt_1} & = & \dfrac{1}{\hat{\tau}}\left(\dfrac{k_2^2}{k_2^2 + Q_c^2 C^2} - r\right) & = & g_2(C, r),\\ \dfrac{dP}{dt_1} & = & \hat{\nu}\left(1 - \dfrac{\alpha}{1 + \frac{Q_c C}{k_4}}\right) - \hat{\beta}\,P & = & g_3(C, P),\end{array}\right. \tag{1}$$

with dimensionless fluxes

$$\begin{aligned}\bar{J}_{\text{release}} &= \frac{k_{\text{flux}}\,\gamma}{V_p}\left(\mu_0 + \mu_1\left(\frac{P}{P + \frac{k_\mu}{Q_p}}\right)\right) r\left(b + V_1\frac{C}{C + \frac{k_1}{Q_c}}\right)(C_t - (1 + 1/\gamma)C),\\ \bar{J}_{\text{serca}} &= \frac{V_e}{V_p}\frac{C}{C + \frac{k_e}{Q_c}},\\ \bar{J}_{\text{pm}} &= \frac{C^2}{C^2 + \frac{k_p^2}{Q_c^2}},\\ \bar{J}_{\text{in}} &= \frac{\alpha_1}{V_p} + \frac{\alpha_2}{V_p}\frac{Q_p\hat{\nu}}{\hat{\beta}}.\end{aligned}$$

The four variables are the non-dimensionalised calcium concentration C in the cytoplasm (reference scale is $Q_c = 1.0\,\mu M$), the non-dimensionalised total calcium concentration C_t in the cell (again, reference scale is $Q_c = 1.0\,\mu M$), the non-dimensionalised IP$_3$ concentration P in the cytoplasm (reference scale is $Q_p = 10.0\,\mu M$), and the fraction r of IP$_3$ receptors (IPR) that have not been inactivated by calcium. The values of the parameters used in (1) are the same as those in [4] and given in Table 1; we work here with the dimensionless parameters $\hat{\tau} = \tau\delta V_p/Q_c$, $\hat{\nu} = \nu Q_c/(Q_p\delta V_p)$, $\hat{\beta} = \beta Q_c/(\delta V_p)$ and $\epsilon = \delta \ll 1$ which is the singular perturbation parameter. The parameter $\hat{\nu}$ is a scaled version of the maximal rate ν of IP$_3$ formation. Experimentally, ν is relatively easily manipulated as it is directly related to the concentration of agonist applied to the cell. We use $\hat{\nu}$ as the primary bifurcation parameter, but also report our results in terms of ν for ease of comparison with earlier work on the Atri model [6].

With the choice of model parameter values as given in Table 1, the dynamics of C is significantly faster than the dynamics of C_t, as is consistent with previous theoretical and experimental work [15]. As argued in [9], the parameters $\hat{\beta}$ and $\hat{\nu}$

parameter	value	parameter	value	parameter	value
b	0.111	k_2	$0.7\ \mu\text{M}$	k_{flux}	$6.0\,\mu\text{M}\,\text{s}^{-1}$
δ	0.01	k_4	$1.1\ \mu\text{M}$	V_p	$24.0\,\mu\text{M}\,\text{s}^{-1}$
γ	5.405	k_p	$0.4\ \mu\text{M}$	V_e	$20.0\,\mu\text{M}\,\text{s}^{-1}$
μ_0	0.567	k_e	$0.06\,\mu\text{M}$	α_1	$1.0\,\mu\text{M}\,\text{s}^{-1}$
μ_1	0.433	k_1	$1.1\ \mu\text{M}$	α_2	$0.2\,\text{s}^{-1}$
V_1	0.889	k_μ	$4.0\ \mu\text{M}$	β	$0.8\,\text{s}^{-1}$

Table 1: Values of parameters for the Atri model (1), which are the same as the values used in [6]. All substrate concentrations are concentrations per liter cytosol, i.e., $\mu\text{M} \equiv \mu\text{M}/(\text{liter cytosol})$.

are $O(1)$ in the parameter domain of interest, so P is a slow variable compared with C. The dynamics of r, the inactivation of the IP$_3$ receptor, is of order $O(1/\hat{\tau})$. If $\hat{\tau} = O(1)$ then r is a slow variable. On the other hand, if $\hat{\tau} = O(\epsilon)$ or less then r is a fast variable.

These two cases have an interpretation in terms of the Class I and Class II models as discussed before. Class I models require a slow negative feedback on the IP$_3$ receptor, which is modelled by r. Therefore, $\hat{\tau} = O(1)$ is a necessary condition and we define a Class I model as (1) with $\alpha = 0$, i.e., no calcium feedback on the IP$_3$ production, and $\hat{\tau} = O(1)$. This leads to a model with one fast (C) and three slow variables (C_t, r, and P). Note that the dynamics of the third slow variable P is decoupled from the others. On the other hand, Class II models abolish the slow negative feedback on the IP$_3$ receptor via a fast (instantaneous) response to calcium concentration in the r-dynamics but include calcium feedback on the IP$_3$ production. Hence, we define a Class II model as (1) with $\alpha \neq 0$ and $0 < \hat{\tau} \ll 1$, which leads to a model with two fast (C, r) and two slow variables (C_t, P). The Hybrid Atri model is then defined as (1) with $\alpha \neq 0$ and $\hat{\tau} = O(1)$ or less, and may have either two or three slow variables, depending on the order of $\hat{\tau}$.

In all these cases (Class I, Class II or Hybrid) the Atri model (1) has at least two slow variables which makes our geometric singular perturbation analysis presented in [9] significantly different from the presentation in [6] where they only identified one slow variable (C_t). In particular, we were able to explain mixed-mode oscillations (MMOs) [3] observed in Class I and Class II via canard theory [4, 5, 18] and we also identified the necessary time-scale criterion for the r-dynamics to distinguish Class I and Class II models.

1.2 The focus of this work

In this paper, we go a step further with our analysis and consider the response to a pulse of IP_3 in Class I, Class II and Hybrid forms of the Atri model. We use GSPT to investigate the mechanisms underlying the different pulse responses and, in particular, to explain the anomalous delays seen in, for example, Fig. 1(b). In our numerical simulations, we follow [6] and model the pulsing process using the time-dependent function

$$S(t_1) = \hat{M}\, H(t_1 - t_0)\, H(t_0 + \Delta - t_1), \tag{2}$$

which is added to the right-hand side of the equation for P in (1). Here, $\hat{M}$ denotes the pulse magnitude and H is the Heaviside function

$$H(x) = \begin{cases} 0 & \text{if} \quad x < 0, \\ 1 & \text{if} \quad x \geq 0. \end{cases}$$

The pulse is applied at time t_0 and has duration Δ; we used $\hat{M} = 8.33\dot{3}$, $t_0 = 12$ and $\Delta = 0.72$ throughout, which are the values used in [6], after non-dimensionalisation.

We want to point out that the results obtained in [9] for the Class I model are not sufficient to predict the pulsed dynamics for the Class I model or the dynamics of the Hybrid model in the case $\hat{\tau} = O(1)$; in these two cases, a model reduction to two slow variables is not possible and we must study the full four-dimensional system with three slow variables to understand rigorously the observed pulsing behaviour.

Section 2 presents the analysis of the Class I Atri model. Although this system has three slow variables, we show that it has geometric structures similar to the folded singularities found in systems with two slow variables. These results provide the first application of recent work of Wechselberger [14], which extends canard theory to systems with three (or more) slow variables. We identify a one-dimensional set of folded singularities, which consists of segments of folded saddles, folded nodes and folded foci. It is this mix of different types of folded singularities that creates distinct possibilities for anomalous delays observed in certain parameter regimes of the pulsed Class I Atri model; this would be impossible to occur if there are only two slow variables in the model. In particular, we identify two major types of anomalous delays that are predominantly caused by either folded-saddle or folded-node type singularities.

The analysis for the Class II model is done in Section 3. We show in Section 4 that the Hybrid model can exhibit dynamics similar to either the Class I or Class II models, and that the presence or absence of anomalous delays in this case can be understood just as in the Class I and Class II cases.

The relation between earlier work on pulse responses reported in [6] and the results presented here is discussed in detail in Section 5, where we also summarise our results.

2 Dynamics of the Class I Atri model

The Class I Atri model, for which $\alpha = 0$ and $\hat{\tau} = O(1)$ in (1), has one fast variable, namely C, and three slow variables, namely C_t, r and P. Since $\alpha = 0$, the $\dot{P}$-equation decouples from the other variables and P evolves monotonically to its equilibrium value $P = \hat{\nu}/\hat{\beta}$. If one is primarily interested in the long term dynamics of the Class I Atri model, then it suffices to study the three-dimensional slice $\{P = \hat{\nu}/\hat{\beta}\}$ of the (C, C_t, r, P)-space, because all orbits will eventually evolve to this submanifold of phase space. This approach was taken in [9] to study the unpulsed dynamics and we give a brief summary in Section 2.1 including basic concepts from GSPT [4, 5, 18, 19].

In order to understand the transient response to pulsing of IP$_3$, analysis of the full four-dimensional system is necessary. We present these new results about the pulsed Class I Atri model in Section 2.2, where we also describe two mechanisms that explain the anomalous delays sometimes seen in this case.

We use $\hat{\tau} = 0.48$ ($\tau = 2.0$) throughout for the numerical illustrations of the Class I Atri model. Qualitatively similar results are obtained for other choices of $\hat{\tau}$ that are $O(1)$.

2.1 Class I dynamics in the absence of pulsing

If we restrict our attention to the slice $\{P = \hat{\nu}/\hat{\beta}\}$, then the Class I Atri model becomes a system with one fast and two slow variables. The dynamics of such a three-dimensional system can be analyzed using established methods from GSPT [4, 5, 18]. However, we prefer to summarise the results in [9] about the unpulsed Class I Atri model in the context of the full four-dimensional phase space, because this facilitates the extension to the pulsed case.

The dynamics of singularly perturbed systems such as the Atri model (1) frequently consists of a mix of slow and fast motions, with the prototypical example being a relaxation oscillation (RO), i.e., a periodic motion consisting of long periods of small changes interspersed with short periods of large changes in the (fast) state variables. As $\epsilon \to 0$, the corresponding trajectory converges during slow motions to solutions of the singular limit system of (1) which is a differential algebraic system called the *reduced problem*. Here, the algebraic constraint $f(C, C_t, r, P, 0) = 0$ defines

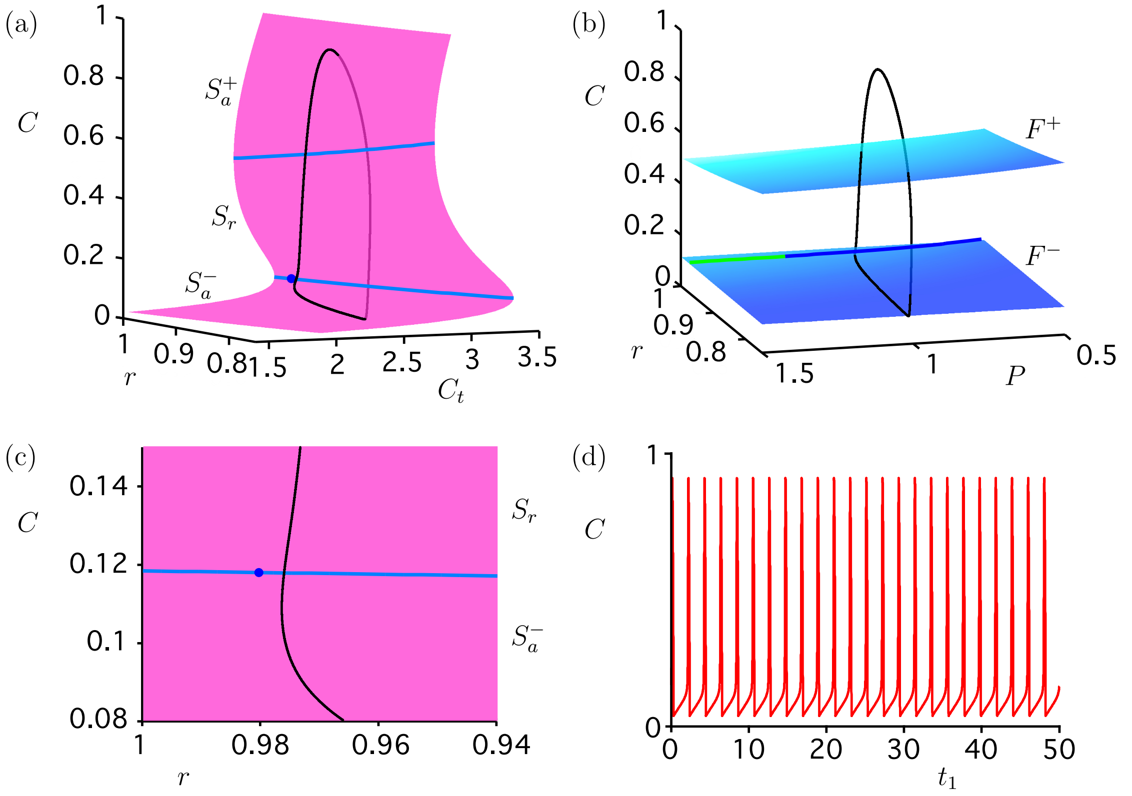

Figure 2: An example of an attracting RO for the Class I Atri model with $\epsilon = 0.01$ and $\hat{\nu} = 0.317$ ($\nu = 0.76$). The slow and fast segments of the RO (black curve) can be explained using the critical manifold, as explained in the text. (a) Using (C_t, r, C) coordinates, with P fixed at the equilibrium value, $P = \hat{\nu}/\hat{\beta} = 0.95$. The pink surface is the intersection of the critical manifold with the slice, and the blue curves are the intersections of the fold surfaces with the slice. The blue dot marks the folded-focus singularity that occurs for this value of P. (b) Projection onto (P, r, C) coordinates. The blue surfaces are the fold surfaces $F^{\pm}$; on these surfaces the C_t-coordinate appears as a colour gradient (dark to light as C_t increases). The green and dark-blue curve is the locus of folded singularities; blue indicates a folded focus, green indicates a folded node, consistent with the colour coding of singularities in Fig. 3. The black curve is the RO shown in panel (a). (c) An enlargement of panel (a) showing the passage of the RO past the folded-focus singularity. (d) The time series for C corresponding to the RO in panel (a).

a three-dimensional (hyper)surface S_0 which is the phase space for the three slow variables (C_t, r, P). As described in [9], S_0 is given as a graph over (C, r, p)-space as can partially be seen in Fig. 2(a) which shows S_0 for $\hat{\nu} = 0.317$ ($\nu = 0.76$) restricted to the slice $\{P = \hat{\nu}/\hat{\beta}\}$ in (C, r, C_t)-space. The critical manifold is S-shaped and this is also the case for other values of P. Hence, there are two fold surfaces, $F^{\pm}$, in the full four-dimensional space, as shown in Fig. 2(b) in projection onto (C, P, r)-space. The colour gradient on these surfaces indicates the value of C_t, ranging from 2.1 (light) to 3.5 (dark). The fold surfaces separate S_0 into three, three-dimensional sheets, $S_a^{\pm}$ and S_r; the outer two sheets, $S_a^{\pm}$, are attracting and the inner sheet, S_r, is repelling.

During fast motions, the trajectory of an RO converges to solutions of the layer problem, which is obtained by first switching to the fast time scale $t_2 = t_1/\epsilon$ in (1) and then taking the singular limit $\epsilon \to 0$. This gives a simple one-dimensional system for the evolution of the fast variable C while the slow variables (C_t, r, P) are constant. Note that the three-dimensional manifold S_0, the phase space of the reduced problem, is a manifold of equilibria for the layer problem and defines the interface between the two sub-systems. Motion towards or away from S_0 in the layer problem is along one-dimensional fast fibres.

The switching between slow and fast motion happens at the fold surfaces $F^{\pm}$. Starting from F^- at relatively low C-values, near the blue dot in Fig. 2(a), the RO makes an almost vertical jump away from S_0, with a corresponding sharp peak in the time series in Fig. 2(d). As soon as the orbit reaches the attracting sheet S_a^+ of S_0, the motion becomes slow again and follows S_0 back to the other fold surface F^+, after which another near-vertical jump occurs to the other attracting sheet S_a^- of S_0. In Fig. 2(b) we cannot see the attracting sheets $S_a^{\pm}$, but we can clearly distinguish the near-vertical jumps in the fast C-direction. Observe how the orbit passes the upper fold surface F^+ in Fig. 2(a) on its way to S_a^+. This is not a true intersection but appears to be so only due to the projection of four-dimensional phase space. A similar observation can be made at the lower fold surface F^- in Fig. 2(b).

Figure 2 clearly shows the power of singular perturbation theory, namely the ability to concatenate solution segments of the lower-dimensional limiting problems, the one-dimensional layer and the three-dimensional reduced problem, to obtain an approximate solution of the full four-dimensional model. Here, the layer problem is particularly simple, since it is only one dimensional, and so we focus solely on analysing the three-dimensional reduced problem. By definition, the reduced vector field has to be in the tangent bundle of the critical manifold S_0. As described before, S_0 is given as a graph over (C, r, p)-space. Hence we would like to study the reduced flow in the single (C, r, p)-chart which covers the whole manifold. Taking the total time derivative of $f(C, C_t, r, P, 0) = 0$ defines a vector field for C that is constrained to the tangent bundle of S and leads to the reduced problem projected onto the base (C, r, P),

$$\begin{cases} -f_C \dfrac{dC}{dt_1} &= f_{C_t} g_1 + f_r g_2 + f_P g_3, \\ \dfrac{dr}{dt_1} &= -g_2, \\ \dfrac{dP}{dt_1} &= -g_3, \end{cases} \tag{3}$$

where $(C, C_t, r, P) \in S_0$ and $f_C = \partial f / \partial C$, $f_{C_t} = \partial f / \partial C_t$, etc. This system is singular along the fold surfaces $F^{\pm}$, where $f_C = 0$. To understand the reduced flow completely, we rescale time by the factor $-f_C$ which gives the *desingularized problem*

$$\left\{ \begin{array}{rcl} \dot{C} & = & f_{C_t} g_1 \;+\; f_r g_2 \;+\; f_P g_3, \\ \dot{r} & = & -f_C g_2, \\ \dot{P} & = & -f_C g_3 \,, \end{array} \right. \tag{4}$$

where the overdot denotes, for convenience, differentiation with respect to the new rescaled time. The reduced flow is equivalent to the desingularized flow up to a time parametrization change on the repelling sheet S_r where $f_C > 0$, i.e., one only has to reverse the direction of the desingularized flow on S_r to obtain the corresponding reduced flow. We distinguish two types of singularities in the desingularized problem (4):

- *Ordinary singularities* are defined by $g_1 = g_2 = g_3 = 0$ away from the fold surface, i.e., $f_C \neq 0$.

- *Folded singularities* are defined by $f_C = 0$ and $f_{C_t} g_1 + f_r g_2 + f_P g_3 = 0$, and represent a one-dimensional sub-manifold of singularities on the fold-surface $f_C = 0$.

Ordinary singularities correspond generically to isolated equilibrium points of the reduced problem (3). Here we have a single equilibrium which is a stable node on the lower sheet of S_a for $0 < \hat{\nu} < 0.144$ ($0 < \nu < 0.345$), a saddle on the middle sheet S_r for $0.144 < \hat{\nu} < 3.34$ ($0.345 < \nu < 8.02$), and again a stable node but on the upper sheet S_a for $\hat{\nu} > 3.34$ ($\nu > 8.02$). GSPT predicts that, for sufficiently small $\epsilon > 0$, these hyperbolic equilibria (away from the fold-surfaces) persist as true equilibria of the full system. In the case of a stable node, this equilibrium corresponds to the only stable attractor of the system.

In the case of the (unstable) saddle equilibria, there exist stable attractors other than equilibria and the folded singularities become important objects in determining these attractors. It turns out that, at the values of $\hat{\nu}$ of interest, only one of the two fold surfaces of S_0 contains such folded singularities, namely, the fold surface F^- with the lowest C-values, as indicated in Fig. 2(b). These folded singularities all have one zero eigenvalue since there is a curve of folded singularities. The corresponding eigenvector of each of these folded singularities is tangent to the curve of folded singularities. The other two eigenvalues vary as we move along the curve of folded singularities. Following the general canard theory developed in [19] and by

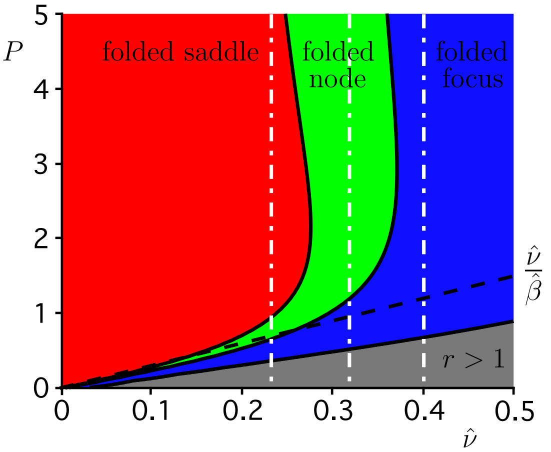

Figure 3: Classification of folded singularities on the fold surface F^- of S_0 in the Class I Atri model for a range of values of $\hat\nu$. For each $\hat\nu$, there exists a curve of folded singularities parametrised by P. The type of the folded singularities are indicated by the colours red, green and blue, for folded saddle, folded node and folded focus, respectively. The grey shaded region consists only of folded singularities with $r > 1$, which is unphysical. The equilibrium value of $P = \hat\nu/\hat\beta$ (black dashed line) indicates at which folded singularity the attractor passes the fold surface. The white dashed lines indicate the values of $\hat\nu$ used for Figs. 6, 7 and 9 (from right to left).

analogy with canard theory for the case of two slow variables, we classify these singularities according to the signs of their non-zero eigenvalues. A folded singularity with two negative real eigenvalues (and one zero eigenvalue) is called a *folded node*, a singularity with two real eigenvalues of opposite sign is called a *folded saddle*, and a singularity with a complex conjugate pair of eigenvalues with non-zero real part is a *folded focus*. Figure 3 shows the types of folded singularities seen in the Class I Atri model for a range of $\hat\nu$-values by assigning a colour to the P-coordinate associated with each singularity; we colour folded saddles red, folded nodes green and folded foci blue.

Note that folded singularities do not correspond to equilibria of the reduced flow (3). In the case of a folded saddle or folded node, the role of the folded singularity is to provide a mechanism by which orbits of the reduced flow on the outer sheet S_a^- may reach the folded singularity in finite time and then cross to the repelling inner sheet S_r. For $\epsilon \neq 0$, this leads in the case of a folded node to local oscillatory behaviour as shown in Fig. 4(c); see, e.g., [19] for theoretical background.

The dynamics of the full (i.e., nonsingular) unpulsed Class I system can now be understood in terms of these geometric structures. Since we are not interested in transient behaviour in the unpulsed case, the relevant folded singularity is that which occurs at the equilibrium value of P for the $\hat\nu$ value of interest; this $\hat\nu$-dependent line of singularities is indicated by the dashed black line in Fig. 3. We find that

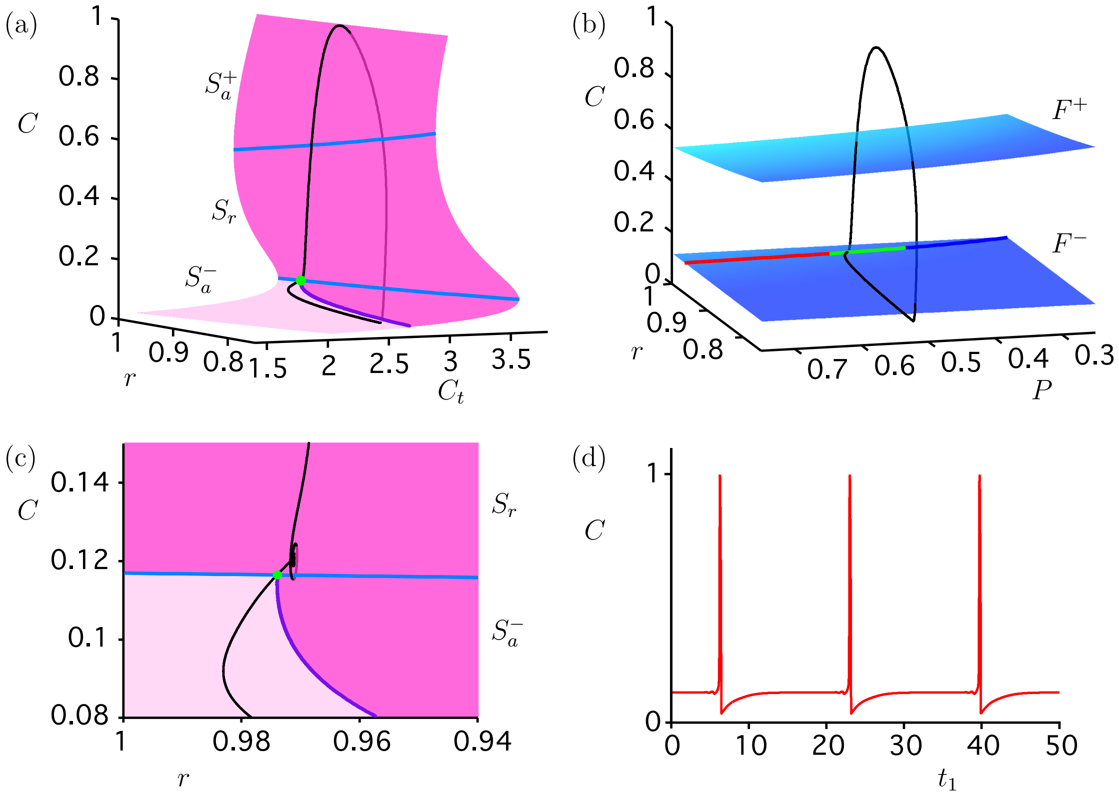

Figure 4: An example of an attracting MMO for the Class I Atri model with $\epsilon = 0.01$ and $\hat{\nu} = 0.167$ ($\nu = 0.40$). (a) Using (C_t, r, C) coordinates, with P fixed at the equilibrium value, $P = \hat{\nu}/\hat{\beta} = 0.50$. The pink surface is the intersection of the critical manifold with the slice, with the light pink section indicating the funnel region of the folded node (green dot) that occurs for this value of P. The blue curves are the intersections of the fold surfaces with the slice. (b) Projection onto (P, r, C) coordinates. The blue surfaces are the fold surfaces $F^{\pm}$; on these surfaces the C_t-coordinate appears as a colour gradient (dark to light as C_t increases). The red, green and dark-blue curve is the locus of folded singularities; red indicates a folded saddle, blue indicates a folded focus, green indicates a folded node, consistent with the colour coding of singularities in Fig. 3. The black curve is the MMO shown in panel (a). (c) An enlargement of panel (a) showing the passage of the MMO past the folded-node singularity. (d) The time series for C corresponding to the MMO in panel (a).

the singularity at $P = \hat{\nu}/\hat{\beta}$ is a folded saddle for $\hat{\nu} \in [0.0, 0.144]$ ($\nu \in [0.0, 0.345]$), a folded node for $\hat{\nu} \in [0.144, 0.259]$ ($\nu \in [0.345, 0.623]$), and a folded focus for $\hat{\nu} > 0.259$ ($\nu > 0.623$).

GSPT predicts that, for sufficiently small $\epsilon > 0$, the attractor in the region with $\hat{\nu} < 0.144$ ($\nu < 0.345$) and $\hat{\nu} > 3.34$ ($\nu > 8.02$) is the stable node equilibrium (as explained above). In the case $3.34 > \hat{\nu} > 0.259$, we have a saddle on the repelling inner sheet S_r and a folded focus on F^-. GSPT predicts in this case a stable RO as the attractor. The equilibrium value $P = \hat{\nu}/\hat{\beta}$ for the case shown in Fig. 2 lies in the blue region of Fig. 3 and the enlargement in Fig. 2(c) shows that the periodic orbit is, indeed, an RO.

In the case $0.114 < \hat{\nu} < 0.259$, there is a saddle on the repelling inner sheet S_r and a folded node on F^-. GSPT predicts here either MMO or RO in the full system, depending on the global return mechanism [4, 5]. Specifically, we expect that the attractor will be an MMO periodic orbit, provided the passage near the folded node leads to a global return into the *funnel region* of the folded node; this is precisely what happens for the case shown in Fig. 4. Detailed calculations shown in Fig. 7 of [9] provide ϵ-dependent boundaries of the MMO regime. In the case $\epsilon = 0.01$, this is given by $0.158 < \hat{\nu} < 0.259$ ($0.38 < \nu < 0.63$). For larger values of $\hat{\nu}$ the return is outside the funnel and the attractor will be a periodic orbit of ordinary RO type.

The type of attractor that occurs in the Class I Atri model without pulsing is qualitatively the same for any sufficiently small value of ϵ, i.e., the attractor is either a stable node, an MMO or an RO, with the boundaries of the intervals of $\hat{\nu}$ on which each type of attractor occurs being only slightly changed by the size of ϵ.

2.2 Class I dynamics with pulsing

The insight gained from the analysis of the unpulsed Class I model yields an explanation for the different types of transient responses seen in the pulsed Atri Class I model. Note that the long term behaviour of the pulsed model is just as for the unpulsed model, i.e., equilibria, MMOs or ROs may be observed, depending on the sizes of $\hat{\nu}$ and ϵ.

The effect of a pulse of IP$_3$ is to send an orbit rapidly to a high value of P, with the precise location after the pulse depending on the pulse size and on the position of the orbit immediately before the pulse. Since the evolution of P is independent of the other variables in the Class I model, the P component of the orbit will then relax to its equilibrium value, but during this relaxation the other variables will evolve in a more complicated way. Figure 5 shows three different possibilities, corresponding to three representative values of $\hat{\nu}$. The pulse response in Fig. 5(a), for $\hat{\nu} = 0.4$ ($\nu = 0.96$), exhibits a small transient increase in frequency of oscillation followed by smooth re-establishment of the attracting RO. This is accompanied by a small decrease in oscillation amplitude, which is not significant. Figure 5(b) shows the response for $\hat{\nu} = 0.317$ ($\nu = 0.76$). Here we observe MMO-like behaviour that causes relatively long delays between peaks during the transient part, but then the orbit settles back to the expected RO for this $\hat{\nu}$-value. The response in Fig. 5(c) for $\hat{\nu} = 0.233$ ($\nu = 0.56$) is expected to relax to an MMO, but we observe a very long delay before the oscillation restarts.

The full three-dimensional critical manifold S_0 plays an important role in our

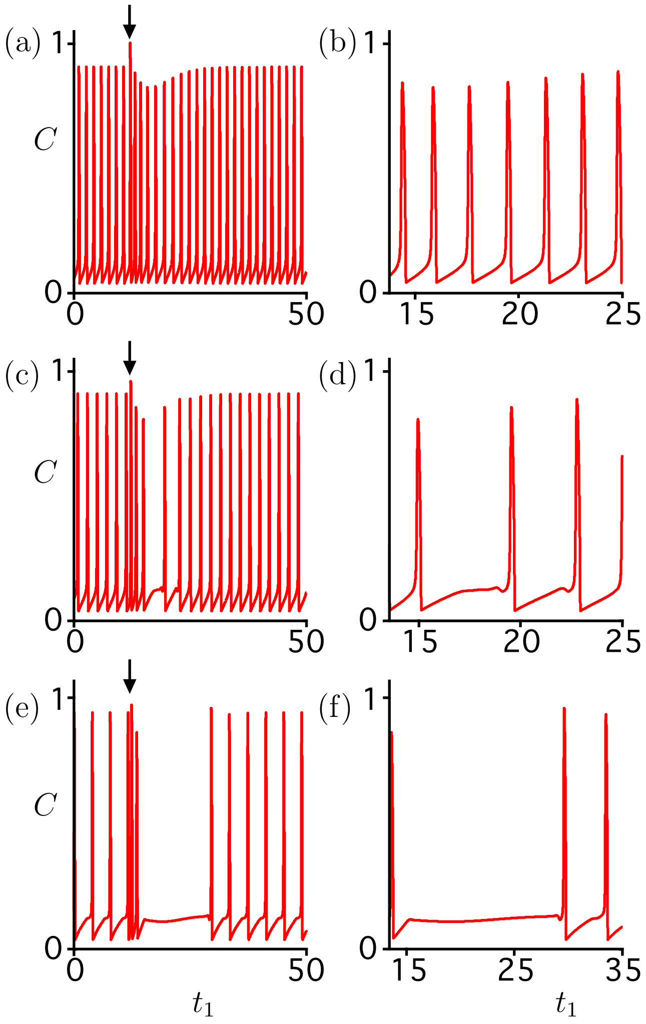

Figure 5: Time series of the C-coordinate for the pulsed Class I Atri model with $\epsilon = 0.01$. Panels (a), (c) and (e) show the responses for $\hat{\nu} = 0.400$ ($\nu = 0.96$), $\hat{\nu} = 0.317$ ($\nu = 0.76$) and $\hat{\nu} = 0.233$ ($\nu = 0.56$), respectively; these values correspond to the white dashed vertical lines in Fig. 3. Enlargements of the transient behaviour after the pulse is applied at $t_1 = 12$ (and once P has decayed to $P = 5$) are shown in panels (b), (d) and (f). The time intervals shown in the enlargements correspond to the orbit segments plotted in the phase portraits shown in Figs. 6, 7 and 9.

explanation of the pulse response of the Class I Atri model, as do the two-dimensional fold surfaces and the curves of folded singularities. We already introduced these structures in the previous section and refer, in particular, to Fig. 3, where the three cases corresponding to Fig. 5 are indicated by white dashed vertical lines at the respective $\hat{\nu}$-values. Since P is no longer fixed for the pulsed Class I Atri model, we always show in the figures that follow two projections, namely, onto (C, r, C_t)-space and onto (C, P, r)-space. In each projection we also plot the two fold surfaces $F^{\pm}$ with the curve of folded singularities of S_0. The fourth missing coordinate in each

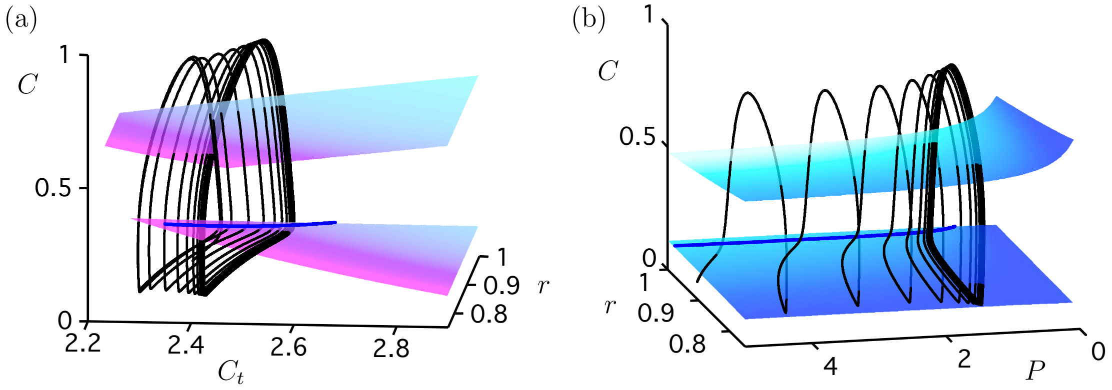

Figure 6: RO-like transient behaviour for the pulsed Class I Atri model with $\hat{\nu} = 0.4$ ($\nu = 0.96$) and $\epsilon = 0.01$. Panels (a) and (b) show projections onto (C_t, r, C)-space and (P, r, C)-space, respectively. The two fold surfaces are shown, with a colour gradient indicating the value of the missing fourth coordinate; P ranges from 5 (pink) to 0 (cyan) in panel (a) and C_t ranges from 2.2 (dark) to 3.5 (light) in panel (b). The curves of folded singularities are also shown, with the colour indicating the type of folded singularity as in Fig. 3. The corresponding time series for the orbit is shown in Fig. 5(a).

projection is indicated by a colour gradient on the fold surfaces. We use dark (low) to light (high) for C_t, as before, and pink (high) to cyan (low) for P.

After the pulse, the orbit typically will not be near S_0 and the first behaviour observed is, therefore, typically a fast transition to an attracting sheet of S_0, after which the evolution is (approximately) dictated by the slow flow on S_0 until the orbit meets a fold surface. This typically occurs at a regular jump point, so that the orbit continues with a fast jump to the other attracting sheet of S_0. As a consequence we observe a large RO in the transient dynamics.

We observe a series of such transient oscillations in the time series in Fig. 5(a), where $\hat{\nu} = 0.4$ ($\nu = 0.96$). The corresponding phase portrait is shown in Fig. 6; panel (a) shows the projection onto (C, r, C_t)-space and panel (b) onto (P, r, C)-space. Note that the curve of folded singularities consists only of folded foci (blue) for this $\hat{\nu}$-value; see Fig. 3. Fold points in a neighborhood of a folded focus are regular jump points. Hence, each time the fold-surface is reached near such a folded focus a regular fast jump happens. By identifying the near-vertical transitions from the fold surface F^- in Fig. 6, we can identify the sequence of jump points on this fold surface. Both for the transient and the long term dynamics, we see that the orbit interacts with the fold surface F^- at regular jump points and the oscillations are all of RO type. We remark that the decrease in oscillation amplitude that is observed to accompany the increase in frequency after the pulsing in Fig. 5(a) is a consequence of the two fold surfaces $F^{\pm}$ being closer together at higher values of P. A similar comment applies to the other times series in Fig. 5, although the

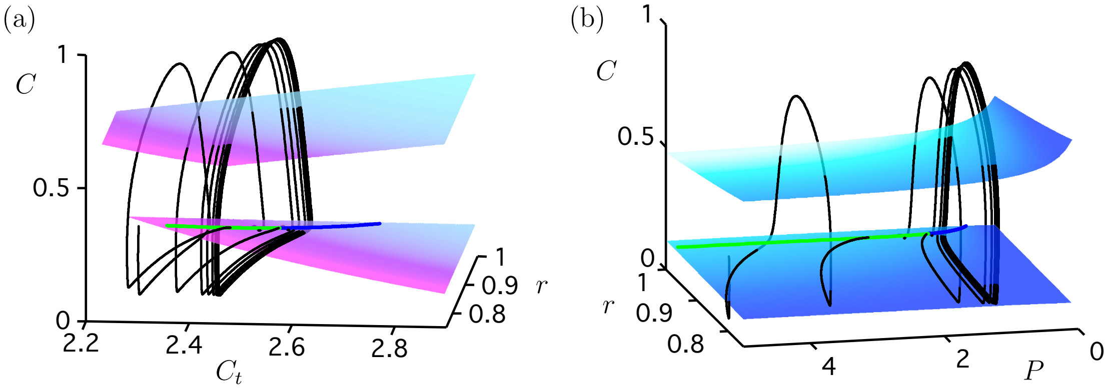

Figure 7: MMO-like transient behaviour for the pulsed Class I Atri model with $\hat{\nu} = 0.317$ ($\nu = 0.76$) and $\epsilon = 0.01$. Panels (a) and (b) show projections onto (C_t, r, C)-space and (P, r, C)-space, respectively. The two fold surfaces and folded singularities are shown with colouring as in Fig. 6. The corresponding time series for the orbit is shown in Fig. 5(c).

phenomenon is less easily seen in those cases.

2.2.1 Anomalous delay due to interaction with a folded node

The time series in Fig. 5(c), where $\hat{\nu} = 0.317$ ($\nu = 0.76$), shows oscillations immediately after the pulsing similar to the case shown in Fig. 5(a), but the initial increase in frequency is followed by a relatively long delay before the orbit returns to its unpulsed oscillation, which is of RO-type for this $\hat{\nu}$-value. Note the small-amplitude oscillations visible in the enlargement in Fig. 5(d) before the third and fourth spikes. As indicated in Fig. 3, the folded singularities on S_0 are no longer all folded foci; for high P-values the singularities are folded nodes and the associated funnel region on S_0 forms a three-dimensional sectorial trap that the orbit is likely to meet as P decreases from a high value after pulsing. Passage through a folded node leads to MMO-like oscillations in the transient orbit; the orbit has a quiescent period as it moves through the funnel region on S_a^- towards the curve of folded-node singularities on F^-, then small oscillations occur near F^- followed by a fast jump towards S_a^+. The transient orbit may return to the three-dimensional funnel region and again pass through another folded node at a smaller value of P, until P has decreased to values where the funnel ceases to exist because the folded singularities are of folded-focus type.

Figure 7 shows two projections of the phase portrait for the case with $\hat{\nu} = 0.317$ ($\nu = 0.76$). The MMO-like transient behaviour occurs each time the orbit reaches the fold surface F^- at a (green) folded node. We observe that the pulsed orbit first crosses the fold surface F^- at a jump point, but after the fast jump the orbit falls into the funnel region for the segment of folded-node singularities and the second

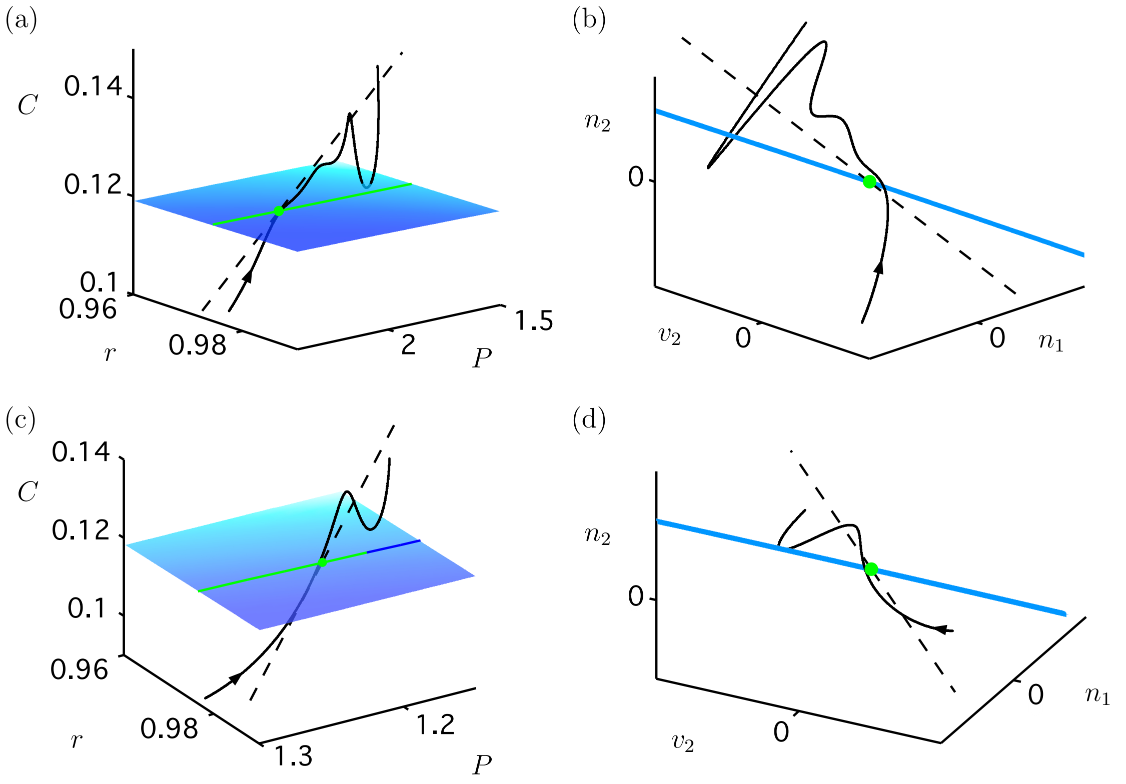

Figure 8: The enlargement of segments of the pulsed orbit plotted in Fig. 7(b) near the second (a) and third (b) crossing of the fold surface shows the interaction with the curve of folded nodes. The second column shows a projection along the vector direction associated with the zero eigenvalue of the folded node, such that the fold surface is almost one dimensional.

crossing of the fold surface F^- is at a folded node.

Panels (a) and (b) in Fig. 8 show a close-up of the passage through the folded-node segment at this second crossing; panel (a) is an enlargement near the folded node in the same projection as Fig. 7(b), and panel (b) shows the projection along the vector $\mathbf{v}_1$ associated with the zero eigenvalue of the folded node involved in this second crossing. The coordinate axes are aligned with the vector $\mathbf{v}_2$ that is tangent to the fold surface but orthogonal to $\mathbf{v}_1$, and with two additional vectors $\mathbf{n}_1$ and $\mathbf{n}_2$ normal to the fold surface. The projection in Fig. 8(b) shows oscillating behaviour that is reminiscent of a passage through a folded node for a three-dimensional system with two slow variables [4, 5, 18].

The third crossing of the fold surface by the orbit in Fig. 7(b) is also at a folded node, and a close-up for this crossing is shown in Fig. 8(c), with an enlargement in Fig. 8(d). After this third crossing, P has decreased so much that the type of folded singularities changes to folded foci (blue segment) and the transient orbit (as well as the long term behaviour) thereafter looks like an RO.

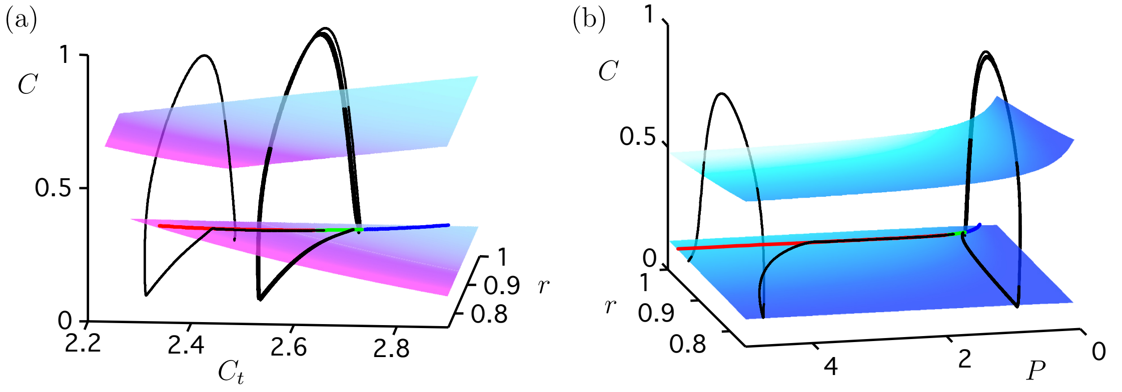

Figure 9: Dynamics of the pulsed Class I Atri model with $\hat{\nu} = 0.233$ ($\nu = 0.56$) and $\epsilon = 0.01$, showing one orbit after pulsing (black curve). (a) Projection onto (C_t, r, C) coordinates. At the equilibrium value of P, the folded singularity is a folded node. (b) Projection onto (P, r, C) coordinates. All surfaces and curves as in Fig. 6. A time series for the orbit is shown in Fig. 5(c).

The pulse response of the model at this value of $\hat{\nu}$ can therefore be characterised as being a few RO-type oscillations of greater frequency and smaller amplitude than the attracting RO, followed by a number of MMO-like oscillations (each including a delay then some small-amplitude oscillations then a fast jump) before re-establishment of the RO. We note that the number and amplitude of the ROs immediately after the pulsing and before the delay, as well as the length of the delay and the number of small-amplitude oscillations during the transient may depend on factors such as the location in phase space of the orbit immediately before pulsing, the length and magnitude of the applied pulse and on the exact $\hat{\nu}$ value, but the underlying mechanism described here is robust.

We have, thus, identified a mechanism causing anomalous delays in the pulse response of the Class I Atri model: a ‘delay’ before resumption of ROs can occur as the transient orbit after a pulse passes through the funnel region associated with a segment of folded-node singularities on the stable sheet S_a^- of the critical manifold. Note that the trapping region of the folded-node segment, the funnel, causes a delay effect because orbits on S_a^- slow down as they move to and along the weak eigendirection of the folded nodes. Furthermore, orbits have to make a certain number of small-amplitude oscillations near the folded nodes before they ultimately get ‘ejected’ from the funnel.

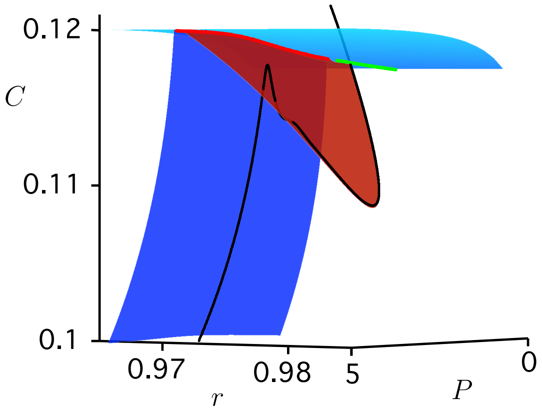

Figure 10: Enlargement of Fig. 9, showing the stable (dark-blue) and unstable (dark-red) manifolds of the curve of folded saddles, as well as the pulsed orbit (black) as it passes through this region. The stable and unstable manifolds and the fold surface (light blue) all intersect at the curve of folded singularities (shown in light red and green).

2.2.2 Anomalous delay due to interaction with a segment of folded saddles

The anomalous delay seen in the pulse response of the Class I Atri model, as shown in the time series in Fig. 5(c), is caused by a second different mechanism, namely by passage near a segment of folded-saddle singularities. We have found that a one-dimensional family of folded saddles can also provide a trapping region for the slow flow. Such a trapping region is bounded by the two-dimensional families of stable and unstable manifolds of the folded saddles. Unlike the funnel region for a segment of folded nodes, the families of (un)stable manifolds each form two-dimensional surfaces on S_a^- that prevent orbits from reaching the fold-surface F^- and ultimately force solutions away from F^- on S_a^-. The unstable manifolds are often compact on S_a^-, because they can bend back and connect to folded nodes in a neighbouring segment. This offers an escape from the trapping region, because solutions will leave a neighbourhood of the folded saddles along the unstable eigendirection of the folded saddles, until P eventually gets small enough that the folded singularities change to folded-node type. As soon as the orbit escapes from its ‘trap’, a jump is observed in the transient orbit.

An example of this type of behaviour is shown in Fig. 9, for the case $\hat{\nu} = 0.233$. Both projections show that the pulsed orbit passes near F^-, lingering very close to the segment of folded saddles. Fig. 10 shows an enlargement of part of Fig. 9(b), but projected onto (P, r, C)-space, so that F^- appears horizontal. This figure also shows the two-dimensional surfaces formed by the one-dimensional stable (blue) and one-dimensional unstable (red) manifolds of the segment of folded saddles. The pulsed orbit enters this region near the surface of stable manifolds. As it comes close to the fold surface F^- and the curve of folded saddles, it is pushed away along the surface of unstable manifolds and remains trapped on S_a^- until it reaches the segment of folded nodes. Note that, for this model at least, passage near a segment of folded saddles followed by a segment of folded nodes produces a more lengthy delay than passage through a segment of folded nodes only.

3 Dynamics of the Class II model

A Class II model is defined as (1) with $\alpha \neq 0$ and $0 < \hat{\tau} \ll 1$. Hence, the r-dynamics is considered fast which leads to a model with two fast (C, r) and two slow variables (C_t, P). As explained in [9], it is possible to make a quasi-steady-state approximation of the r-variable by letting $\hat{\tau} \to 0$ and setting

$$r(C) = \frac{k_2^2}{k_2^2 + C^2},$$

in which case system (1) effectively becomes three dimensional, with one fast variable and two slow variables:

$$\begin{cases} \epsilon \dot{C} &= \bar{J}_{\text{release}} - \bar{J}_{\text{serca}} + \epsilon(\bar{J}_{\text{in}} - \bar{J}_{\text{pm}}) =: \tilde{f}(C, C_t, P, \epsilon), \\ \dot{C}_t &= \bar{J}_{\text{in}} - \bar{J}_{\text{pm}} = g_1(C), \\ \dot{P} &= \hat{\nu}\left(1 - \frac{1}{1+C/k_4}\right) - \hat{\beta}P =: g_3(C, P). \end{cases} \tag{5}$$

Standard techniques from GSPT were used in [9] to analyze this system, and the main results from that paper are summarised in the following section.

3.1 Class II dynamics in the absence of pulsing

The constraint $\tilde{f}(C, C_t, P, 0) = 0$ defines the critical manifold, S_0, of system (5). The constraint equation can be solved for C_t as a function of C and P; the resultant surface is plotted in Fig. 11. An important feature of S_0 is that it has two fold curves (relative to C) for $P < 0.45$, with the folds merging in a cusp at $P \approx 0.45$. In the region $P < 0.45$, the manifold is S-shaped, with the outer sheets $S_a^{\pm}$ of S_0 (corresponding to larger and smaller values of C) being attracting and the inner sheet S_r (corresponding to intermediate values of C) being repelling. For $P > 0.45$ the single sheet S_a of S_0 is attracting. As usual, the critical manifold can be thought of as organising the dynamics of (5) in the sense that, for sufficiently small ϵ, solutions of (5) will alternate between spending relatively long periods of time near S_0 and

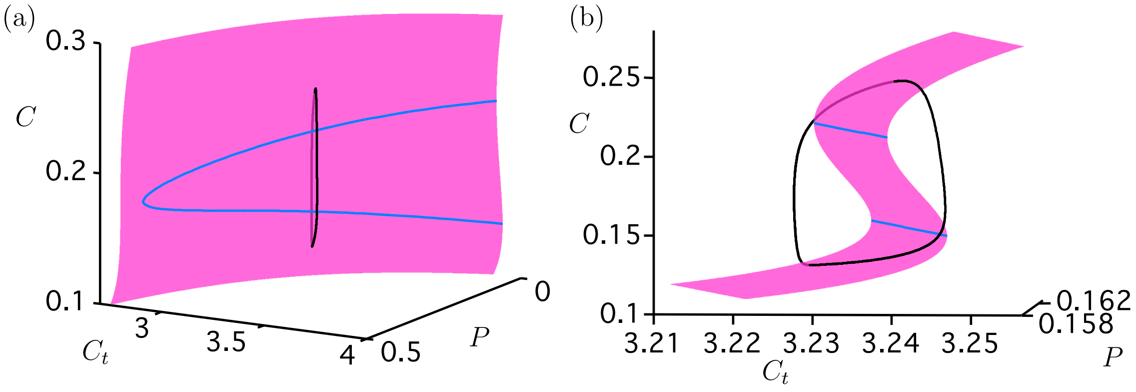

Figure 11: The critical manifold for the Class II Atri model (5) and the attracting RO that occurs when $\epsilon = 0.001$ and $\hat{\nu} = 0.417$ ($\nu = 1.0$). (a) The critical manifold is shown in pink, and has two fold curves for $P < 0.45$ (blue curves). These curves merge in a cusp point at $P \approx 0.45$. The black curve shows the attracting RO. (b) An enlargement of panel (a) from a different view point, illustrating the S-shape of the critical manifold.

making fast jumps between different sheets of S_0.

As discussed in [9], for most values of $\hat{\nu}$ in the interval $[0.311, 0.629]$, solutions are attracted to an RO like that shown in Fig. 11. This is the case even though there are folded-node singularities on the fold curves of S_0, because the global dynamics forces orbits away from the regions near the folded singularities. For ϵ sufficiently small there can be a very small interval of $\hat{\nu}$ near $\hat{\nu} = 0.629$ where orbits are attracted to a folded node and MMOs are observed, but this is of no further interest here. Outside the interval $[0.311, 0.629]$, solutions are attracted to a stable node.

For the purposes of understanding the response of the Class II model to IP$_3$ pulses, a little more detail about the folded-node singularities is helpful. This detail does not affect the long term behaviour of solutions to this model but does have implications for the transient behaviour immediately after a pulse, as discussed in the next section. Figure 12 shows some features of the critical manifold for two representative choices of $\hat{\nu}$. For $\hat{\nu} \in [0.311, 0.446]$ the strong canard for the folded node on the lower fold curve bends around and joins again to the fold curve, meaning that the folded node is inaccessible unless an orbit starts in the funnel region which is bounded by the strong canard and the fold curve. This situation is illustrated in Fig. 12(a). In contrast, for $\hat{\nu} \in [0.446, 0.629]$ the strong canard does not meet the lower fold curve except at the folded node, and the associated funnel region is open. In this case the funnel region attracts the flow from the upper right part of the phase space; see Fig. 12(b).

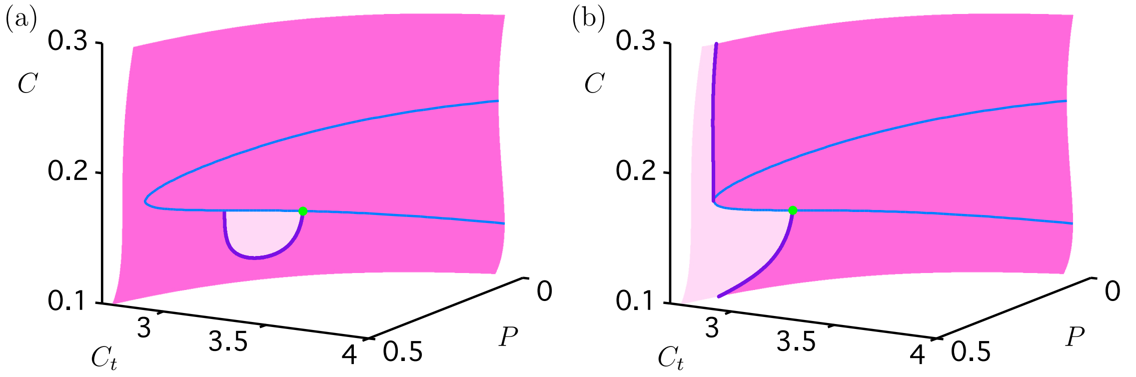

Figure 12: Dynamics on the critical manifold for the Class II Atri model (5), for two values of $\hat{\nu}$: (a) $\hat{\nu} = 0.417$ ($\nu = 1.0$); (b) $\hat{\nu} = 0.542$ ($\nu = 1.3$). The critical manifold is pink and the fold curves are blue. The green dots show the location of folded-node singularities and the purple curves emanating from the folded nodes are the associated strong canards. The light-pink region is the funnel region for the folded node. In (a), the funnel region is bounded by the lower fold curve and the strong canard. In (b), the funnel region is an open region of the critical manifold.

3.2 Class II dynamics with pulsing

Due to the three-dimensional nature of the Class II system, any delays such as that seen in Fig. 1(c) must be explained by a completely different mechanism than those used for the Class I model. Nevertheless, we can still use the geometric structures found in the analysis of the unpulsed Class II system. An IP$_3$ pulse applied to this model moves an orbit rapidly to higher values of P (i.e., past the cusp). For small ϵ, orbits will first move quickly towards the critical manifold then follow the slow flow on the critical manifold until a fold curve is encountered, after which the orbit could make a fast jump. Since there are no folds in the critical manifold for large P there can be no fast jumps and hence no oscillations initially. Eventually, the value of P will decrease sufficiently that the orbit returns to the folded section of the critical manifold and then eventually to the attracting RO which occurs for low values of P. This explains the observed delay in the onset of oscillations after the pulse – until P is small enough there can be no oscillations.

The details of the evolution once P is small enough for the critical manifold to be folded ($P < 0.45$) depend on details of the folded singularities described above. For $\hat{\nu} < 0.446$ ($\nu < 1.07$), the funnel region (when it exists at all) is completely bounded by the fold curve and strong canard, and so a transient orbit cannot enter the region. Instead the pulsed orbit goes below the funnel region and settles down to the RO. On the other hand, if the funnel region is open ($0.446 < \hat{\nu} < 0.629$, i.e., $1.07 < \nu < 1.51$) then a pulsed orbit will typically return to the attractor via the funnel of the folded node. This results in small oscillations in the transient

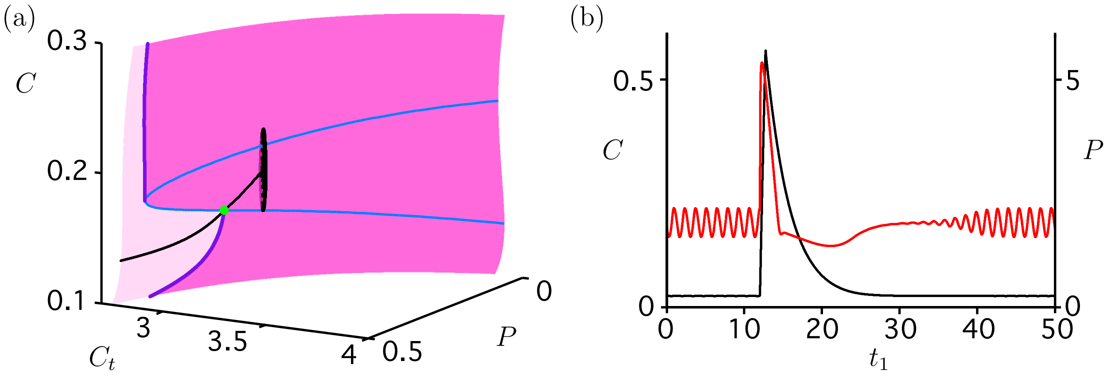

Figure 13: Dynamics for the Class II Atri model (5) with $\hat{\nu} = 0.542$ ($\nu = 1.3$) and $\epsilon = 0.01$. (a) All curves and surfaces are as in Fig. 12, except that the black curve shows a trajectory after the application of an IP_3 pulse. After the pulse, the trajectory passes the cusp point on the fold curves, then passes through the funnel region towards the folded node, resulting in a delay followed by characteristic small oscillations before re-establishment of the RO. (b) Time series for the orbit shown in (a). The red curve shows C and is plotted against the left vertical axis. The black curve is P and is plotted against the right vertical axis.

orbit before RO are established again. Figure 13 confirms this prediction in the case $\hat{\nu} = 0.542$ ($\nu = 1.30$).

4 Dynamics of the Hybrid model

The Hybrid Atri model is obtained by setting $\alpha \neq 0$ and $\tau \neq 0$ in equations (1). This system may have either two fast and two slow variables or one fast and three slow variables, depending on the relative size of $\hat{\tau}$. A comprehensive analysis of the Hybrid Atri model was not presented in [9], either for unpulsed or pulsed versions of the model, since GSPT relevant to systems with three slow variables had not been developed when [9] was written. In this section we argue that when $\hat{\tau} = O(1)$ the dynamics of the Hybrid model has many qualitative features of the pure Class I model. As a consequence, the pulse response of the Hybrid model is, for these values of $\hat{\tau}$, similar to the pulses response of the Class I model. In particular, the delay sometimes seen after pulsing of the Hybrid model when $\hat{\tau} = O(1)$ can be attributed to the existence of segments of folded saddles and folded nodes in the singular limit of the Hybrid model. If, on the other hand, $\hat{\tau} \ll 1$, the Hybrid model behaves like a Class II model in both the pulsed and unpulsed dynamics. There is an intermediate range of values of $\hat{\tau}$ where the Hybrid model is in transition between Class I and Class II forms. In this transition regime, GSPT based on the assumption of there being just two distinct time scales in the model is unable to give clear predictions about the behaviour in the model, and numerical investigations indicate that features of

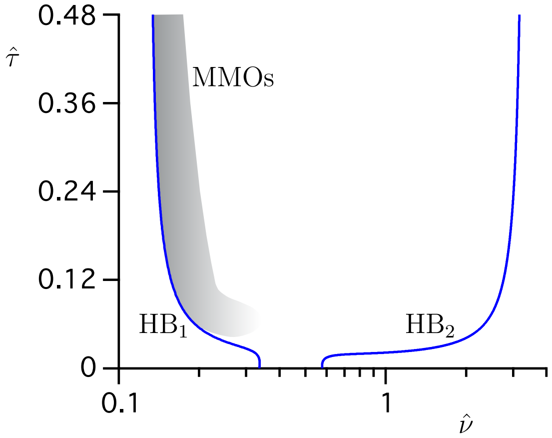

Figure 14: Partial bifurcation set for the Hybrid Atri model, equations (1) with $\epsilon = 0.01$ and various α and $\hat{\tau}$. The locations of Hopf bifurcations (HB) are marked, and the shaded region indicates the values of α and $\hat{\tau}$ for which MMOs are observed. A sharp transition in the slope of the Hopf bifurcation curves occurs at $\hat{\tau} \approx 0.05$ at about the same value of $\hat{\tau}$ where MMOs cease to exist. This value of $\hat{\tau}$ corresponds to the Hybrid model making a transition from having three slow variables ($\hat{\tau} = O(1)$) to having two slow variables ($\hat{\tau} = O(10^{-2})$).

both Class I and Class II dynamics can be observed.

4.1 Hybrid model without pulsing

Analysis of the time scales of the Atri model presented in [9] showed that the Hybrid Atri model might be expected to behave like a Class I model if $\hat{\tau} = O(1)$, and like a Class II model if $\hat{\tau} = O(10^{-2})$. Numerical evidence for a transition regime is contained in Fig. 14, which shows a partial bifurcation set for the Hybrid Atri model in the case that $\epsilon = 0.01$. Oscillations are possible only in the region in between the two curves of Hopf bifurcations, denoted HB$_1$ and HB$_2$ in Fig. 14. These oscillations are of RO type, except in the shaded region, where MMOs exist. A clear transition regime can be seen as $\hat{\tau}$ decreases in Fig. 14. Specifically, at $\hat{\tau} \approx 0.05$ the distance between HB$_1$ and HB$_2$ changes suddenly and the MMO regime terminates.

A detailed investigation of the case $\alpha = 1$, $\hat{\tau} = 0.48$ ($\tau = 2.0$) and $\epsilon = 0.01$, which is a representative parameter choice for which the Hybrid model has three slow variables, provides evidence that there are many features in common between this model and the pure Class I model discussed in the previous section. In the Hybrid model, P does not evolve independently of other variables, with the consequence that the long term dynamics does not lie in fixed-P slices of phase space (as was the case for Class I), but otherwise phase-space plots look rather similar to Figs 2, 4, and 6–9, as will be shown below.

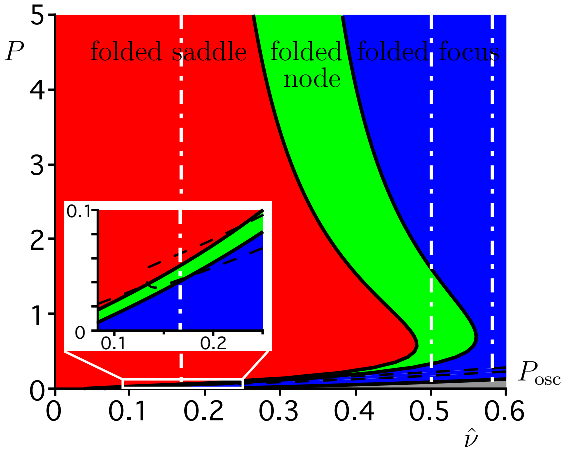

Figure 15: The types of folded singularity seen in the Hybrid Atri model, equations (1) with $\alpha = 1$, $\hat{\tau} = 0.48$ ($\tau = 2.0$) and $\epsilon = 0$, for a range of values of $\hat{\nu}$. The meanings of the colours are as in Fig. 3. The white dashed lines indicate the values of $\hat{\nu}$ used for Figs. 18, 19 and 20. The black dashed curves (labelled $P_{\rm osc}$) for $\hat{\nu} > 0.125$ indicate the maximum and minimum values of P for the attracting closed orbit (MMO or RO) at each value of $\hat{\nu}$. For $\hat{\nu} < 0.125$ the attracting orbit is an equilibrium solution with P value given by the dashed black line. The inset shows an enlargement of the indicated region.

Techniques from GSPT can be applied to the Hybrid model, just as for the Class I model in Section 2. In particular, the three-dimensional critical manifold and the different types of folded singularities that exist can be computed, and singular MMOs can be constructed for a range of values of $\hat{\nu}$ where folded-node singularities occur. Figure 15 shows the types of folded singularity seen in the Hybrid system for various values of $\hat{\nu}$. While the boundaries of the regions of existence of the various types of folded singularities have shifted compared with the Class I case shown in Fig. 3, the similarities are clear. Note that in Class I, the variable P evolves to a single equilibrium value, even if the other variables oscillate as part of an MMO or RO, whereas in the Hybrid model P oscillates slightly when there is an MMO or RO. The range of values of P that occur along the singular closed orbit for each value of $\hat{\nu}$ is indicated by the dashed black curves labelled $P_{\rm osc}$ in Fig. 15.

The geometric structures present in the singular limit perturb in the non-singular case just as they did for Class I. Thus, for instance, intervals of $\hat{\nu}$ for which singular MMOs or ROs occur in the singular limit persist in the non-singular system, with the boundaries of these intervals shifted in an appropriate ϵ-dependent way, just as shown above for Class I.

Figure 16 gives an example of Class I-like behaviour of the Hybrid model, for the choice $\hat{\nu} = 0.167$ ($\nu = 0.40$); for this choice of parameters there is an attracting MMO. There are clear similarities between Fig. 16 and Fig. 4, consistent with our claim that the Hybrid Atri model behaves like a Class I model when $\hat{\tau} = O(1)$.

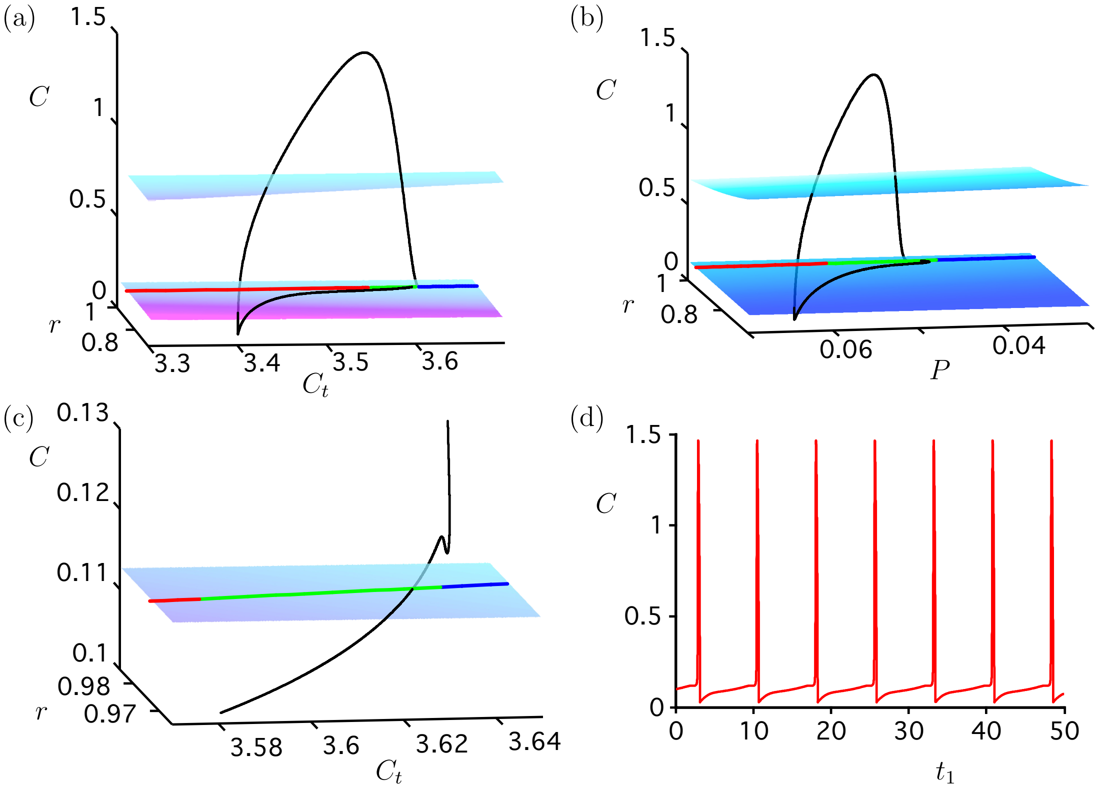

Figure 16: An example of an attracting MMO for the Hybrid Atri model with $\epsilon = 0.01$, $\hat{\nu} = 0.167$ ($\nu = 0.40$) and $\hat{\tau} = 0.48$ ($\tau = 2.0$). Colour coding of surfaces and curves is as in Fig. 6. (a) A projection onto (C_t, r, C) coordinates. (b) The same MMO as in (a) projected onto (P, r, C) coordinates; compare with Fig. 4(b). (c) An enlargement of panel (a) showing the passage of the MMO past the folded-node singularity. (d) The time series for C corresponding to the MMO in (a); compare with Fig. 4(d).

The dynamics of the unpulsed Hybrid model in the case that $\hat{\tau} = O(10^{-2})$ or less is qualitatively like the dynamics for the pure Class II model, but the argument is simpler than for the Class I case: the quasi-steady-state approximation used to reduce the Class II model to a system of three equations in [9] works equally well for the Hybrid model when $\hat{\tau} = O(10^{-2})$ or less and so our description of the Class II model dynamics in Section 3 is valid also for the Hybrid model in this regime.

When $\hat{\tau}$ is of an order intermediate between $O(1)$ and $O(10^{-2})$, then methods of analysis based on the assumption of there being two distinct time scales in the model are no longer appropriate. Result derived for systems with three time scales may be relevant for this transition regime [5, 12] but we do not undertake this kind of analysis here.

4.2 Hybrid model with pulsing

Since the long term dynamics of the Hybrid model can be qualitatively like the dynamics in either the Class I or Class II models, depending on the size of $\hat{\tau}$, it is no surprise that the Hybrid model may respond to a pulse of IP$_3$ in similar ways to the Class I and II models. In particular, we may encounter the same types of anomalous delays as for Class I. Let us illustrate this again using the Hybrid model with $\hat{\tau} = 0.48$ ($\tau = 2$) and $\epsilon = 0.01$. Figure 17 shows three different possibilities, corresponding to three representative values of $\hat{\nu}$; compare with the pulsed responses for the Class I model in Fig. 5.

Figure 18 shows a pulsed orbit in phase space for the Hybrid model when $\hat{\tau} = 0.48$ ($\tau = 2$) and $\hat{\nu} = 0.583$ ($\nu = 1.4$), with the associated time series being plotted in Fig. 17(a). In this case, the unpulsed model is in the Class I regime and we can locate a three-dimensional critical manifold containing a curve of folded singularities. The folded singularities consist of folded foci only and the pulsed orbit meets the fold surface F^- at jump points only. The pulse response for this value of $\hat{\nu}$ is therefore qualitatively similar to that seen in the Class I model with $\hat{\nu} = 0.400$ (see Figs 6 and 5(a)).

Figure 19 shows a pulsed orbit for the Hybrid model when $\hat{\nu} = 0.500$ ($\nu = 1.2$), with the associated time series being plotted in Fig. 17(b). In this case, the first four passages through the fold surface F^- occur at jump points, the next passage is at a folded node, and the orbit eventually settles down to an RO. The pulse response for this value of $\hat{\nu}$ is thus qualitatively similar to the case for the Class I model with $\hat{\nu} = 0.317$; see Figs 7 and 5(b).

Figure 20 shows a pulsed orbit for the Hybrid model when $\hat{\nu} = 0.167$ ($\nu = 0.4$), with the associated time series being plotted in Fig. 17(c). In this case, the pulsed

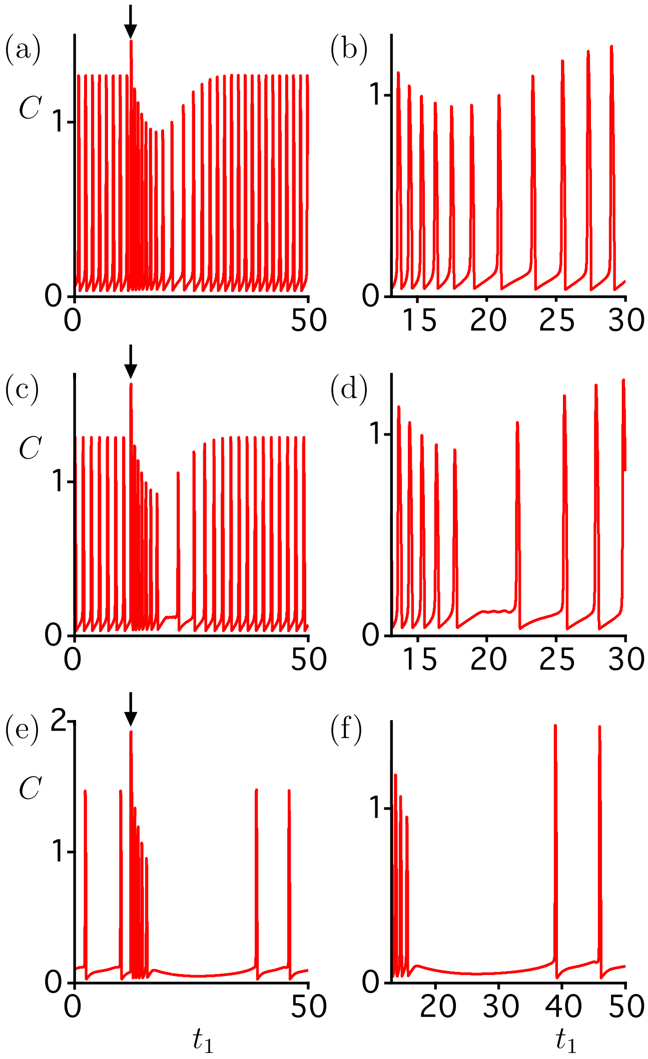

Figure 17: Time series of the C-coordinate for the pulsed Hybrid Atri model with $\alpha = 1.0$, $\hat{\tau} = 0.48$ ($\tau = 2.0$) and $\epsilon = 0.01$. Panels (a), (c) and (e) show the responses for $\hat{\nu} = 0.583$ ($\nu = 1.4$), $\hat{\nu} = 0.500$ ($\nu = 1.2$) and $\hat{\nu} = 0.167$ ($\nu = 0.40$) respectively. These values correspond to the white dashed vertical lines in Fig. 15. Enlargements of the transient behaviour after the pulse is applied at $t_1 = 12$ are shown in panels (b), (d) and (f). The time intervals shown in the enlargements correspond to the orbit segments plotted in the phase portraits shown in Figs 18, 19 and 20.

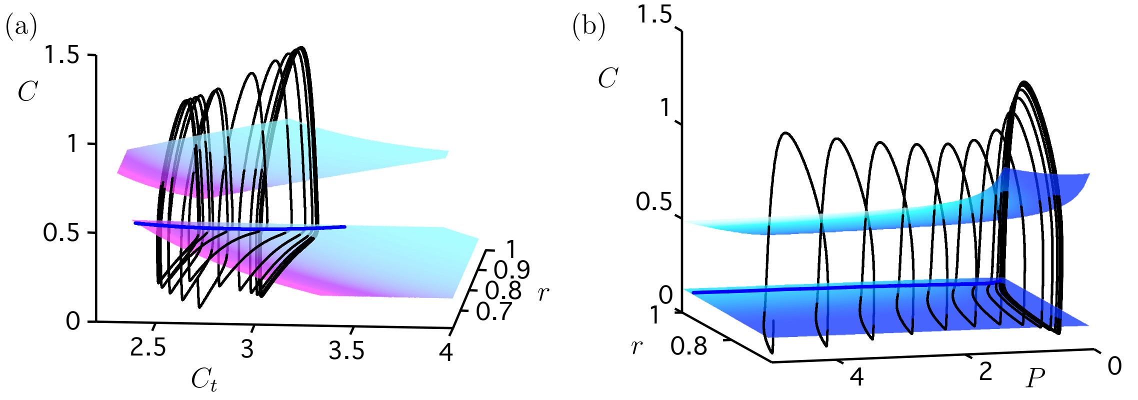

Figure 18: RO-like transient behaviour for the pulsed Hybrid Atri model with $\hat{\nu} = 0.583$ ($\nu = 1.4$), $\alpha = 1.0$, $\hat{\tau} = 0.48$ ($\tau = 2.0$) and $\epsilon = 0.01$. Panels (a) and (b) show projections onto (C_t, r, C)-space and (P, r, C)-space, respectively. All surfaces and curves are as in Fig. 6. All intersections of the orbit with the fold surface occur at jump points. A time series for the orbit is shown in Fig. 17(a).

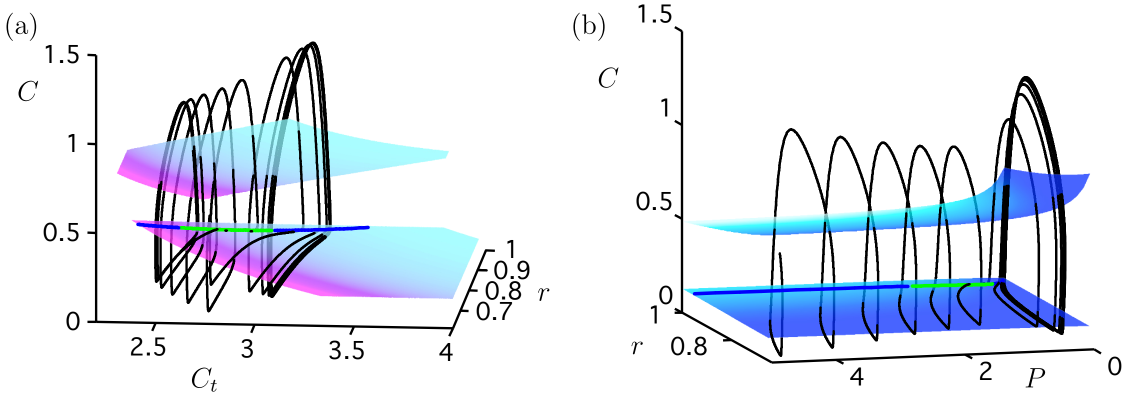

Figure 19: MMO-like transient behaviour for the pulsed Hybrid Atri model with $\hat{\nu} = 0.50$ ($\nu = 1.2$), $\alpha = 1.0$, $\hat{\tau} = 0.48$ ($\tau = 2.0$) and $\epsilon = 0.01$. Panels (a) and (b) show projections onto (C_t, r, C)-space and (P, r, C)-space, respectively. All surfaces and curves are as in Fig. 6. The first four passages through the fold surface are at jump points, the next passage is at a folded node, and the orbit is eventually attracted to an RO (crossing the fold surface at a jump point). A time series for the orbit is shown in Fig. 17(b).

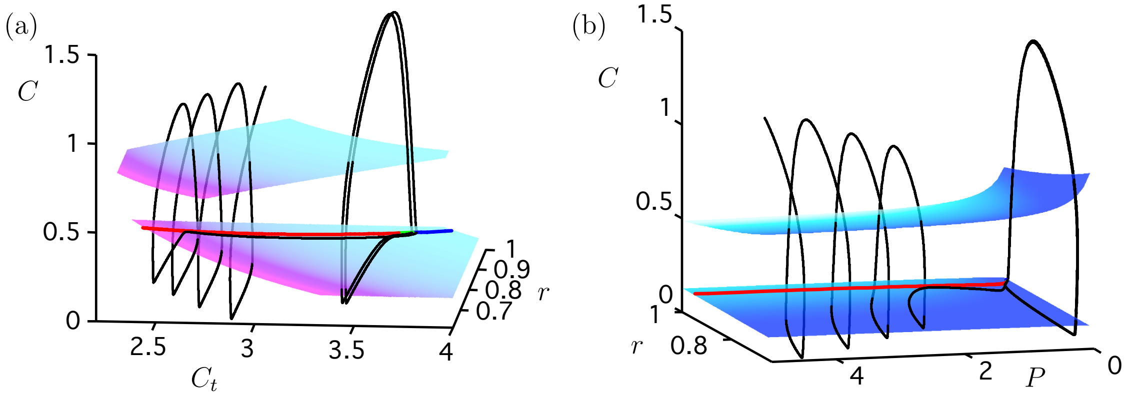

Figure 20: Dynamics for the pulsed Hybrid model with $\hat{\nu} = 0.167$ ($\nu = 0.4$), $\alpha = 1.0$, $\hat{\tau} = 0.48$ ($\tau = 2.0$) and $\epsilon = 0.01$. Panels (a) and (b) show projection onto (C_t, r, C)-space and (C, r, P)-space, respectively. All surfaces and curves as in Fig. 6. The first two passages through the fold surface occur at jump points, then the orbit has a period of drifting along the curve of folded saddles. Eventually the orbit settles down to a MMO, corresponding to passage near a folded node. A time series for the orbit is shown in Fig. 17(c).

orbit makes two passages through the fold surface F^- at jump points, then spends an extended period of time drifting near the segment of folded saddles, then enters the funnel region for the folded nodes, and eventually settles down to an MMO. The pulse response for this value of $\hat{\nu}$ is thus like the case for the Class I model with $\hat{\nu} = 0.233$; see Figs 9 and 5(c).

Hence, we see that the Hybrid Atri model with $\alpha = 1.0$ and $\hat{\tau} = 0.48$ ($\tau = 2.0$) responds to pulses of IP_3 in a qualitatively similar way to the Class I Atri model. Similar results are found for any $\hat{\tau}$ greater than about 0.2.

As argued above, when the Hybrid model is in the Class II regime, i.e., when $\hat{\tau} \ll 1$, the model can be reduced to a three-dimensional model and we find in numerical experiments that pulsing has a similar effect to that seen in the pure Class II model. Specifically, after pulsing there is a delay before re-establishment of oscillations because the pulse pushes the orbit into a region of the phase space where the associated critical manifold has no folds. Oscillations are only re-established once the variable P has decayed enough that the critical manifold is folded.

We have derived no clear theoretical predictions about the response to pulsing for the Hybrid model in the transition regime between the Class I and Class II regimes, but preliminary numerics show that in this case the pulse response has characteristics of both Class I and Class II behaviour. The transition regime is being investigated further and will be reported on elsewhere.

5 Discussion

In this paper, we have used geometric singular perturbation theory (GSPT) to investigate the response of a representative model (the Atri model) of oscillatory calcium dynamics to an exogenous pulse of IP_3. Previous work on this model [6] identified a so-called *anomalous delay* in the transient response of certain versions of the model, specifically in the Class I and Hybrid versions of the model for a range of values of the main bifurcation parameter $\hat{\nu}$, and gave a heuristic explanation for the phenomenon based on a fast-slow decomposition with one slow variable. However, as we have shown, a full analysis of pulsing in the Atri model requires recognition that the model may have two or three slow variables.

Making use of the recent results of Wechselberger [19], which extend canard theory to systems with three or more slow variables, we have shown that the delays sometimes seen in the pulsed Class I and Hybrid versions of the Atri model are associated with the existence of a curve of folded singularities, either folded saddles or folded nodes, in the singular limit of the model. In the parameter regime of interest, the Atri model has periodic attractors, typically of either mixed-mode oscillation (MMO) or relaxation oscillation (RO) type. The effect of pulsing with IP_3 is to move the orbit rapidly away from the periodic attractor to a region of phase space where P is large. The way in which the orbit returns through phase space to the vicinity of the periodic attractor produces the characteristic pulse response of the model, and is heavily influenced by the dynamics of the singular limit of the model of interest, as summarised below.

In the Class I version of the Atri model, P evolves independently of the other variables. After pulsing, P decays monotonically to an equilibrium value while the other variables can oscillate. For sufficiently small values of the singular perturbation parameter ϵ, the transient orbit will alternate between periods when it closely follows the critical manifold of the singular limit system and fast jumps between different sheets of the critical manifold. At larger values of $\hat{\nu}$ where the critical manifold either has no folded singularities or the folded singularities are of folded-focus type, then transient and long term oscillations are of RO type; while the transient orbit might display small changes in frequency or amplitude of oscillation after pulsing, no significant delays are observed in the associated time series. However, at smaller values of $\hat{\nu}$ when the singular limit has folded singularities of folded-node or folded-saddle type, there may be relatively long periods in the transient orbit where there are no oscillations. Sometimes the transient orbit displays MMO-like behaviour including delays and small-amplitude oscillations (when it passes near a segment of folded nodes) and sometimes there is a more lengthy delay (when the orbit passes near a segment of folded saddles) followed by MMO-like transients (near a segment of folded nodes).

Delays are also observed in the pulse response of the Class II Atri model, but in this case they are caused by a completely different mechanism. We showed that, in the parameter regime of interest, the two-dimensional critical manifold for the singular limit of the Class II Atri model has a cusp; for smaller values of P the critical manifold is S-shaped, which means that ROs (and sometimes MMOs) can occur, but at higher values of P the folds merge in a cusp so that the critical manifold is not folded and oscillations do not occur. The effect of pulsing in this case is to send the orbit into the part of phase space where the manifold is not folded. Until the variable P has decayed sufficiently so that the orbit has passed the cusp region and once again gets close to the folded part of the critical manifold, there can be no oscillations. This results in the observed delay in the onset of oscillations after pulsing in the Class II model.

We have argued that the Hybrid Atri model has three regimes: a Class I regime when $\hat{\tau} = O(1)$, a Class II regime when $\hat{\tau} = O(10^{-2})$ or less, and a transition regime for intermediate sizes of $\hat{\tau}$. The form of the pulse response of the Hybrid model is then determined by these regimes: the pulse response is Class I-like if the unpulsed model is in the Class I regime, and is Class II-like if the unpulsed model is in the Class II regime. Features of both the Class I and Class II pulse responses can be seen in the Hybrid model in the transition regime.

A crucial step in understanding the dynamics of the Class I Atri model and of the Hybrid model in the Class I regime was the ability to apply singular perturbation theory to systems with three slow variables. The examples in this paper are the first application of the results in [19] that extend canard theory to the case of three (or more) slow variables. Based on what is seen in systems with two slow variables, it is perhaps not surprising that the presence of folded-node singularities in the singular limit of the Atri model can result in complicated (MMO-like) dynamics. More surprising is the important role played by folded saddles; we found that passage near a segment of folded saddles can result in an extended quiescent period in the time series of a pulsed solution. This trapping region created by the (un)stable manifolds of the folded saddles is only terminated due to a transition in the type of folded singularities – here to folded nodes – and the release is observed as a transient calcium spike due to a jump near a folded node. We note that a passage near a single folded singularity would not produce this effect; this is something that can only occur in systems with three or more slow variables.

A major difference between our analysis of the Atri model and that presented in

[6] is that we have determined that the model can have two or three slow variables, whereas just one slow variable (c_t in the notation of [6]) was used in [6]. As a consequence, some features of the dynamics (such as MMOs) were not identified in [6]. Analysis of the pulse responses for Class I and Hybrid models in [6] implicitly had two slow variables, since p and c_t were treated as parameters, and an association between the location of certain bifurcations of the (two-dimensional) fast subsystem and the transient behaviour of the pulsed orbits was reported. We believe that our use of a singular limit in which there are either three slow variables (for Class I and some Hybrid cases) or two slow variables (for Class II and some Hybrid cases) leads to a clearer explanation of the observed phenomena, including the long term dynamics and the response to pulsing.

The original motivation for studying the response of the Atri model to a pulse of IP_3 was a desire to understand the dynamics behind an experimental protocol proposed in [16]. In the models studied in [16], it seemed that there was a clear difference in the response of different types of model to an IP_3 pulse: Class I models responded with a temporary increase in oscillation frequency while Class II models responded with a phase lag (delay) before re-establishment of oscillations. Thus it was thought that the experimental protocol could be used to determine whether the calcium oscillations in a particular cell type were predominantly determined by Class I or Class II mechanisms. The anomalous delays that are sometimes observed when the Class I Atri model is pulsed have muddled the presumed differences between the response types. In this paper we have identified the mathematical mechanisms behind the varying types of pulse responses; the next steps are to look at other intracellular calcium models, e.g. [7, 13, 14], to determine whether these mechanisms are present, and then to revisit the experimental protocol to see if it can be modified so that its interpretation is unambiguous. Work along these lines is ongoing and will be reported elsewhere.

Finally, we note that identification of the time scales present in the Atri model suggests a mathematical basis for determining whether Class I or Class II mechanisms will drive the oscillations in a Hybrid model that includes both. We conjecture that the dominant mechanism is determined by the relative speed of the receptor dynamics (represented by the variable r in our model); slow receptor dynamics will result in Class I mechanisms being dominant and fast receptor dynamics will result in Class II mechanisms being dominant. This insight into the behaviour of Hybrid models has been confirmed in this paper for the Atri model but results for other models will be reported elsewhere.

References

[1] A. Atri, J. Amundsen, D. Clapham and J. Sneyd. A single-pool model for intracellular calcium oscillations and waves in the *Xenopus laevis* oocyte, *Biophysical Journal* **65**:1727–1739 (1993).

[2] M. J. Berridge, M. D. Bootman and P. Lipp. Calcium - a life and death signal, *Nature* **395**: 645–648 (1998).

[3] M. Brøns, T. Kaper and H. Rotstein (eds.), Focus issue: mixed mode oscillations: experiment, computation, and analysis, *Chaos* **18(1)**: (2008).

[4] M. Brøns, M. Krupa, and M. Wechselberger. Mixed mode oscillations due to the generalized canard phenomenon, *Fields Institute Communications* **49**:39–63 (2006).

[5] M. Desroches, J. Guckenheimer, C. Kuehn, B. Krauskopf, H. M. Osinga and M. Wechselberger. Mixed-mode oscillations with multiple time-scales, *Preprint* (2010).

[6] M. Domijan, R. Murray and J. Sneyd. Dynamical probing of the mechanisms underlying calcium oscillations, *J. Nonlinear Science*, **16**:483–506 (2006).

[7] G. Dupont and C. Erneux. Simulations of the effect of inositol 1,4,5-triphosphate 3-kinease and 5-phosphotase activities on Ca^{2+} oscillations, *Cell Calcium* **22**:321–331 (1997).

[8] N. Fenichel. Geometric singular perturbation theory for ordinary differential equations, *J. Differential Equations* **31**:53–98 (1979).

[9] E. Harvey, V. Kirk, J. Sneyd and M. Wechselberger. Multiple time scales, mixed mode oscillations and canards in models of intracellular calcium dynamics, *Preprint* (2010).

[10] C. K. R. T. Jones. Geometric singular perturbation theory, in *Dynamical systems (Montecatini Terme, 1994)*. Springer-Verlag, Berlin/New York (1995).

[11] J. Keener and J. Sneyd. *Mathematical Physiology*, second edition, Springer-Verlag, New York (2008).

[12] M. Krupa, N. Popovic, and N. Kopell, Mixed-mode oscillations in three time-scale systems: A prototypical example, *SIAM J. Appl. Dyn. Syst.* **7(2)**:361–420 (2008).

[13] Y. Li and J. Rinzel. Equations for InsP_3 receptor mediated $[\mathrm{Ca}^{2+}]_i$ oscillations derived from a detailed kinetic model: a Hodgkin-Huxley like formalism, *J. Theo. Biol.* **166**:461–473 (1994).

[14] A. Politi, L. D. Gaspers, A. P. Thomas and T. Höfer. Models of IP_3 and Ca^{2+} oscillations: Frequency encoding and identification of underlying feedbacks, *Biophysical Journal* **90**:3120–3133 (2006).

[15] J. Sneyd, K. Tsaneva-Atanasova, D. I. Yule, J. L. Thompson and T. J. Shuttleworth. Control of calcium oscillations by membrane fluxes, *PNAS* **101**:1392–1396 (2004).

[16] J. Sneyd, K. Tsaneva-Atanasova, V. Reznikov, Y. Bai, M. J. Sanderson and D. I. Yule. A method for determining the dependence of calcium oscillations on inositol trisphosphate oscillations, *PNAS* **103**:1675–1680 (2006).

[17] P. Szmolyan and M. Wechselberger. Canards in $\mathbb{R}^3$, *J. Differential Equations* **177**:419–453 (2001).

[18] M. Wechselberger. Existence and bifurcation of canards in $\mathbb{R}^3$ in the case of a folded node, *SIAM J. Appl. Dyn. Syst.* **4(1)**:101–139 (2005).

[19] M. Wechselberger. A propos de canards (Apropos canards), *Preprint* (2010).